UNIVERSITÀ DEGLI STUDI DI PADOVA

Dipartimento di Fisica e Astronomia "Galileo Galilei"

Master Degree in Physics

Final Dissertation

Classical and quantum photoemission from N-V centers in nanodiamonds

Thesis supervisor
Prof. Giovanni Mattei
Thesis co-supervisor
Prof. Tiziana Cesca

Candidate
Marco Dassie

Academic Year 2020/2021

ACKNOWLEDGMENTS

I would like to thank professor Giovanni Mattei, professor Tiziana Cesca, doctor Ionut Gabriel Balasa, and the whole NanoStructures Group for their helpfulness and their support throughout my master thesis project.

Contents

Introduction **3**

1 Single photon sources **5**
- 1.1 Figures of merit . . . 5
- 1.2 Hanbury-Brown and Twiss coincidence measurements . . . 8
- 1.3 State of the art . . . 15

2 Nitrogen-Vacancy centers in diamond **21**
- 2.1 Electronic levels . . . 21
- 2.2 Vibronic coupling . . . 30
- 2.3 Neutral NV center and charge dynamics . . . 33
- 2.4 NV synthesis . . . 36
- 2.5 Applications . . . 38

3 Materials and methods **39**
- 3.1 HBT setup . . . 39
- 3.2 Nanodiamonds . . . 48

4 Results and discussion **51**

Conclusions **57**

Introduction

Single photons are currently used in proof of principle experiments [1, 2], as well as in quantum simulation [3], quantum computation [4], and quantum cryptography [5], which are arguably among the most appealing goals for the future information technology. In this context, the single photon source represents a key element, since stringent requirements in terms of photon quality must be fulfilled. Impressive advances have been reported in the last few years, confirmed by the emergence of integrated photonics [6]. However, the scalability of photonic devices and the integration of sources and detectors in the main circuit still poses great challenges.

The first effective approach for producing single photons is found in the nonlinearity of crystals, such as those allowing spontaneous parametric down-conversion. The method takes advantage of the entangled photon pair generation through a heralding mechanism. An alternative solution employs quantum systems whose prototype is the two-level emitter. Again, the nonlinear interaction of a single emitter with the pump pulse is exploited: in an ideal source, no matter how many photons are found in the excitation pulse, the output always consists of a single photon. In practice, such quantum systems can be single atoms, fluorescent molecules, solid state defects, or quantum dots.

Nitrogen-Vacancy (NV) centers as solid state single photon emitters are investigated in this work. Indeed, these defects in diamond have remarkable room temperature emission properties, contrary to most quantum dots, and relatively high brightness, as opposed to heralded single photon sources. In addition, the easiness of fabrication makes them even more appealing.

The aim of the present project is to show the onset of a quantum behaviour in the emission of an ensemble of NV centers in nanodiamonds. Equivalently, the fluorescence should be shown to originate from very few centers by photon coincidence counting. This is the first step towards the development of a solid state single photon source that possibly requires little fabrication and operation resources in order to allow scalability and integration.

The thesis is organized as follows:

- an overview of single photon sources can be found in chapter 1. Particular emphasis is put on the time coincidence measurement for the evaluation of single photon purity, which is central to this work;

- Nitrogen-Vacancy (NV) centers in diamond are introduced in chapter 2. A general outline of all the aspects that might be relevant to the experimental activity of the thesis is given. This includes a brief summary of the electronic and vibronic properties, the charge and spin dynamics, the current fabrication methods and applications;

- the experimental setup for time coincidence detection, along with the measurement details, is described in chapter 3;

- finally, the results obtained for NV lifetime and, more importantly, two-photon time coincidences are discussed in chapter 4. In this context, an estimate of the degree of quantum emission, namely, on the number of centers generating fluorescence photons is presented.

Chapter 1

Single photon sources

Single photon sources have attracted considerable interest in the past two decades. As anticipated, the most popular application is in quantum information, that is, quantum cryptography, quantum simulation and quantum computation. Quantum cryptography [7], for example, leverages pure quantum states of single photons to securely transfer an encryption key. Each information bit can be stored in the degrees of freedom of one photon, such as polarization or spatial position. An eavesdropper trying to obtain this information through a photon measurement would unavoidably destroy the original quantum state, making the transmitter and receiver aware of its presence. An intrinsically secure communication would be possible only with perfect single photon purity (SPP), since any two-photon state carrying one bit of information is a potential source of leakage. As a result, a source of high quality single photons is required.

As for quantum information processing, single photons are promising candidates to prove quantum supremacy over classical algorithms in boson sampling simulations [8]. Furthermore, coherent quantum interaction between single photons and solid state qbits establishes an interface between light and matter that allows promising quantum information transfer [9, 10].

In this section an overview is provided of existing single photon sources, along with their figures of merit. A subsection is dedicated to the Hanbury-Brown and Twiss (HBT) measurement, which plays a major role in this work.

1.1 Figures of merit

Single Photon Purity Single Photon Purity (SPP) is the first parameter to look at when assessing the quality of a single photon source. As mentioned above, it is the foundation of quantum cryptography security, but it is strictly necessary in quantum information processing as well. In this respect, an optimal source would emit one photon at a time, so that it is impossible to detect two photons at zero

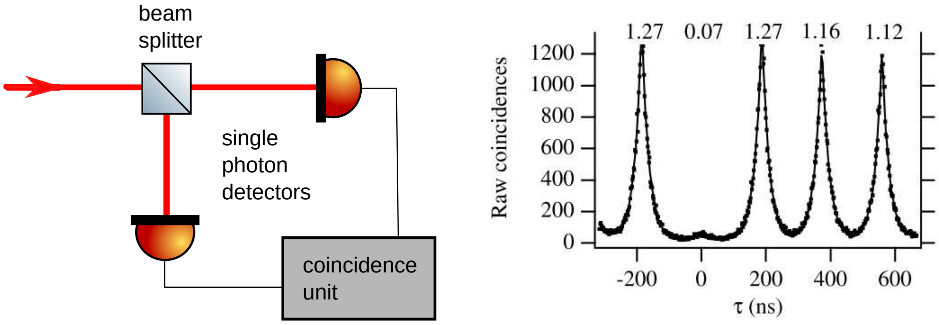

(a)

(b)

Figure 1.1: (a) Scheme of the Hanbury-Brown and Twiss (HBT) setup for photon time coincidence measurements, and (b) coincidence histogram (second order correlation function) of the photoemission from a single NV center with pulsed excitation [11]. The numbers at the top represent the integrals of the peaks beneath.

time separation. As a consequence, time coincidences are measured through the Hanbury-Brown and Twiss setup to quantify single photon purity (see figure 1.1).

Brightness and deterministic generation In addition, photons for quantum information must be generated on-demand (i.e., deterministically). This is in contrast with the probabilistic nature of quantum emission. However, almost deterministic generation can be reached through pulsed excitation of an ideal quantum system: the emitter must be excited with certainty, but just once per laser pulse; then, by controlling the timing of excitation pulses, single photons can be generated on-demand with lifetime-limited uncertainty. In this context, the brightness of the source is usually defined as the average number of single photons impinging on the first optical element per excitation pulse, in order to make it independent from the setup efficiency [14].

Indistinguishability Finally, in quantum computation and simulation, indistinguishability between photons is required. This means that the quantum state of two consecutive photons, or two photons from equivalent sources, must be perfectly symmetric with respect to particle exchange. As a consequence, when meeting at a properly engineered beam splitter, they produce an entangled state by quantum interference (see figure 1.2). This effect is named after Hong, Ou, and Mandel (HOM) [13], who first explored it as a tool for subpicosecond time resolution. Indistinguishability can be evaluated through the Hong-Ou-Mandel Visibility ($0 < \text{HOMV} < 1$); other applications include quantum simulations [8] and quantum sensing experiments [15].

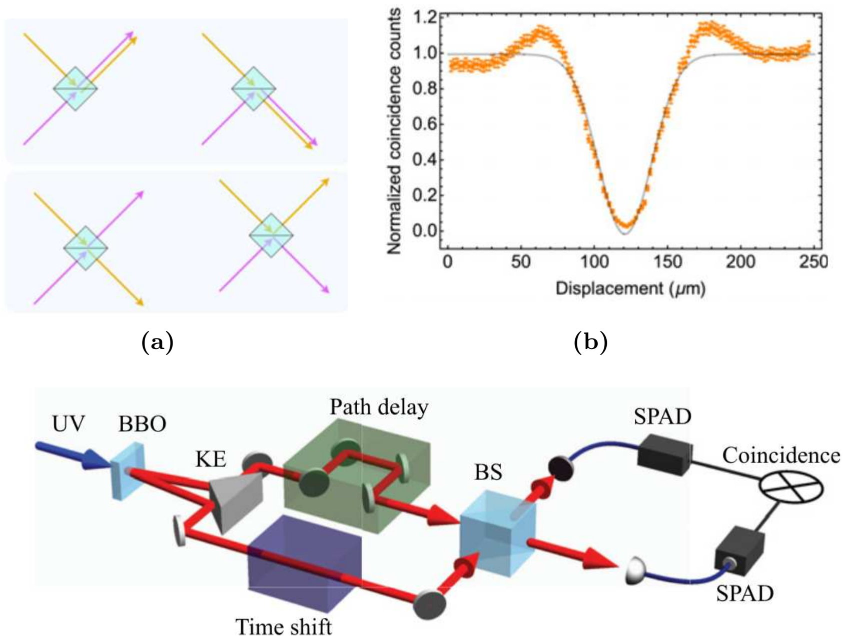

(a) **(b)**

(c)

Figure 1.2: Representation of the Hong-Ou-Mandel (HOM) interference between two indistinguishable photons [12]. In (a) the four possible outcomes of the simultaneous arrival of two photons (orange and violet) at a beam splitter are sketched. The photons are made distinguishable by orthogonal polarization or spectral differentiation, for example. On the contrary, if the incoming photons are perfectly identical, and the beam splitter reflection shifts each photon phase by $\pi/2$, the two output states with a single photon per exit destructively interfere, so that the only possibility is that the photons leave the beam splitter in the same direction. The result is an entangled state in the form $1/\sqrt{2}(|top\rangle\,|top\rangle + |bottom\rangle\,|bottom\rangle)$. The successfulness of HOM interference is seen in the lack of coincidences between output events in the two arms when the input photons are made to overlap in time (b). In (c) a scheme of the setup for HOM coincidence measurement is reported. Hong-Ou-Mandel Visibility (HOMV) can be used as an estimate of the indistinguishability; it is defined as HOMV$= (R_\perp - R_{||})/R_\perp$, where $R_{\perp(||)}$ is the coincidence rate in the orthogonal (parallel) polarization case. The sensitivity to a time shift between the two photons can be exploited for timing measurements with sub-picosecond resolution [13].

1.2 Hanbury-Brown and Twiss coincidence measurements

The Hanbury-Brown and Twiss (HBT) setup consists of a pair of single photon detectors located at the two exit ports of a beam splitter, as can be seen in figure 1.1a; the aim is to measure coincidences in the arrival time of photons.

Classical regime In a classical context, since count rates can be interpreted as intensities, the number coincidences with a specified delay τ, normalized to its infinite delay value (independent events), corresponds to the second order correlation function, that is,

$$g^{(2)}(\tau) := \frac{\langle I(t)I(t+\tau)\rangle}{\langle I(t)\rangle \langle I(t+\tau)\rangle} \tag{1.1}$$

where $I(t)$ is the intensity of the field at time t, and for stationary processes averages are usually intended to be over t. In this picture $g^{(2)}(\tau) \equiv 1$ if $I(t)$ is perfectly constant over time, as in the case of a coherent laser beam, whereas a peak centered in $\tau = 0$ can be seen if intensity fluctuations are present. The temporal width of such peak corresponds to the typical fluctuation time of $I(t)$.

The case of a random electric field described by complex gaussian statistics is often cosidered. In this picture the field values at times t_1, ..., t_N are described by correlated gaussian random variables; the closer the sampling t_i, the more correlated the variables. With matrix notation

$$\underline{E} = \begin{pmatrix} E^{(r)}(t_1) \\ E^{(i)}(t_1) \\ E^{(r)}(t_2) \\ E^{(i)}(t_2) \\ ... \\ E^{(i)}(t_N) \end{pmatrix} \tag{1.2}$$

$$p(\underline{E}) = \frac{1}{(2\pi)^N |\underline{\underline{A}}^{-1}|^{1/2}} e^{-\frac{1}{2}\underline{E}^T \underline{\underline{A}} \underline{E}} \tag{1.3}$$

where $E^{(r)}(t_i)$ and $E^{(i)}(t_i)$ are respectively the real and imaginary part of the electric field at time t_i, $\underline{\underline{A}}$ is the inverse of the covariance matrix, and $p(\underline{E})$ is the probability density function. According to the complex gaussian moments theorem [16]

$$g^{(2)}(\tau) = \frac{\langle E^*(t)E^*(t+\tau)E(t+\tau)E(t)\rangle}{\langle E^*(t)E(t)\rangle \left\langle E^*(t+\tau)E^{(}t+\tau)\right\rangle} \tag{1.4}$$

$$= \frac{\langle E^*(t)E(t+\tau)\rangle \langle E^*(t+\tau)E(t)\rangle + \langle E^*(t)E(t)\rangle \langle E^*(t+\tau)E(t+\tau)\rangle}{\langle E^*(t)E(t)\rangle \left\langle E^*(t+\tau)E^{(}t+\tau)\right\rangle} \tag{1.5}$$

$$= |g^{(1)}(\tau)|^2 + 1 \tag{1.6}$$

Ultimately, the second order correlation function $g^{(2)}(\tau)$ can be written in terms of the first order correlation function $g^{(1)}(\tau)$. Moreover we obtain $g^{(2)}(0) = 2$ and $g^{(2)}(\infty) = 1$, corresponding respectively to maximally correlated and non-correlated fields.

The classical phenomenon that gives rise to a peak in $g^{(2)}(\tau)$ at zero time separation is called bunching: in fact, the beam can be described as a stream of photons temporally grouped in bunches. This feature was first observed by Hanbury-Brown and Twiss, who exploited it in astronomical radiation detection to resolve signals originating from angularly close sources [17].

Bunching observation Although any thermal source is expected to show bunching behaviour, the latter was first observed for a true black body in 2009 [18]. The reason is that, as described by equation 1.6, the bunching feature width is approximately equal to the first order coherence time $t_{coh} = 1/\Delta\nu$, where $\Delta\nu$ is the source bandwidth; on the other hand, $g^{(2)}(\tau)$ is smoothed within the minimum resolution time of the detectors Δt_{det}. As a result, the true peak heigth at zero delay $g^{(2)}(0) - 1$ is reduced to $t_{coh}/\Delta t_{det}\left(g^{(2)}(0) - 1\right)$ in coincidence measurements. Typical detector resolution is in the order of $\Delta t_{det} \sim 100\,\mathrm{ps}$, whereas an equal coherence time $t_{coh} \sim 100\,\mathrm{ps}$ corresponds to a 10 GHz bandwidth source, and is much lower ($< 1\,\mathrm{ps}$) for broadband thermal light. This is why bunching could initially be measured with narrow band emission from Hg lamps [17][19] but not from ordinary thermal sources.

The idea of Boitier et al. [18] is to exploit intrinsically high time resolution from two-photon absorption processes in order to measure femtosecond-scale features in $g^{(2)}(\tau)$. Their results are reported in figure 1.3, along with the experimental setup. The typical coherence time of a 3000 K black body is in the order of 10 fs.

Quantum regime An opposite behaviour can be seen when dealing with quantum sources, whose prototype is a two-level single emitter. In this case the coincidence measurement must be described according to the quantum formalism of creation and annihilation operators:

$$g^{(2)}(\tau) := \frac{\left\langle \hat{a}^\dagger(t)\hat{a}^\dagger(t+\tau)\hat{a}(t+\tau)\hat{a}(t)\right\rangle}{\langle \hat{a}^\dagger(t)\hat{a}(t)\rangle \langle \hat{a}^\dagger(t+\tau)\hat{a}(t+\tau)\rangle} \tag{1.7}$$

This definition can be obtained by applying the normal ordering operator to the classical $g^{(2)}(\tau)$, that is, by moving all annihilation operators to the right of creation ones. The formula describes the probability of detecting both a photon at time t and a photon at time $t + \tau$, normalized by its value at $\tau \to \infty$, that is where the two events are assumed to be independent. Averages are meant over a quantum statistical ensemble, but in practice it is customary to average over time t, since this is closest to the measurement protocol in stationary conditions such as in continuous wave (CW) excitation.

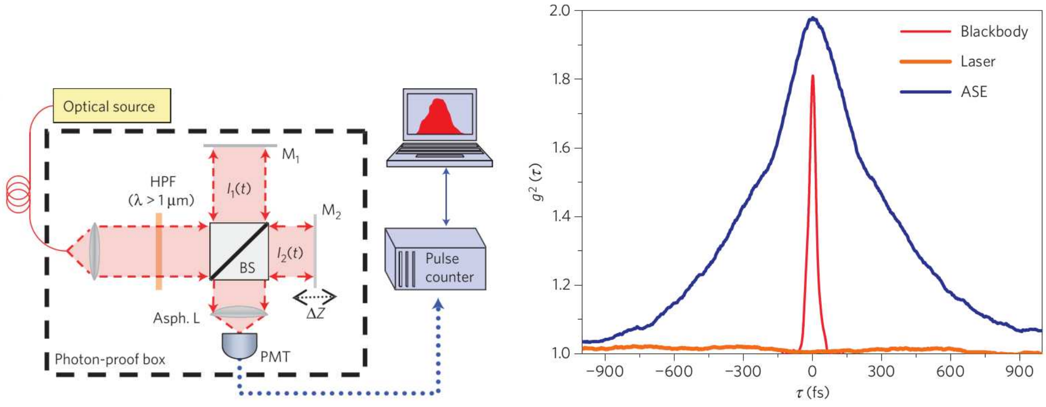

(a) **(b)**

Figure 1.3: Coincidence measurement via two-photon absorption [18]. (a) Experimental setup: light is sent through a High Pass Filter (HPF) to a Michaelson interferometer. The detector is a GaAs Photomultiplier Tube (PMT) working in the two-photon absorption regime for $\lambda > 1\,\mu\text{m}$. (b) Second order correlation function of a diode laser at $\lambda = 1.55\,\mu\text{m}$, an Amplified Spontaneous Emitter (ASE) consisting of an Er^{3+} doped optical fiber, and a 3000 K black body. The classical bunching curve, with maximum value $g^{(2)}(0) = 2$, can be appreciated. A completely incoherent visible-IR source, such as the black body, has typical correlation times of few tens of fs, as can be estimated from the width of the peak.

The main quantum feature (antibunching) in the second order correlation function comes from the fact that it is not possible for an emitter to simultaneously generate two photons. Indeed, the system needs to be pumped again to the excited level after emitting one photon by radiative decay; this requires some time, which depends also on the excitation power. As a result, with an ideal single quantum emitter, no coincidences at zero time separation can be detected (see figure 1.1b for pulsed mode and figure 1.5 for CW mode), whereas the emission of a second photon at large τ is not affected by the emission of the photon at $\tau = 0$; in other words, $g^{(2)}(0) = 0$, and $g^{(2)}(\infty) = 1$. No classical explanation can be provided to account for $g^{(2)}(0) < 1$.

Three-level systems The real emitter often has more than two levels. This is why the second order correlation function sometimes shows an additional bunching feature besides the antibunching dip, as in figure 1.5. However, its explanation is totally unrelated to classical bunching. In fact, the effect can only be seen in the quantum regime (that is, with very few emitters), and is accounted for by rate equations describing the emitter dinamics. Intuitively, the electron, or more generally the emitter, can be shelved in a third level with non negligible lifetime, accessible from the first excited state (respectively levels 3 and 2 in figure 1.4). The time spent in the shelving level reduces the average decay rate between the first excited and the

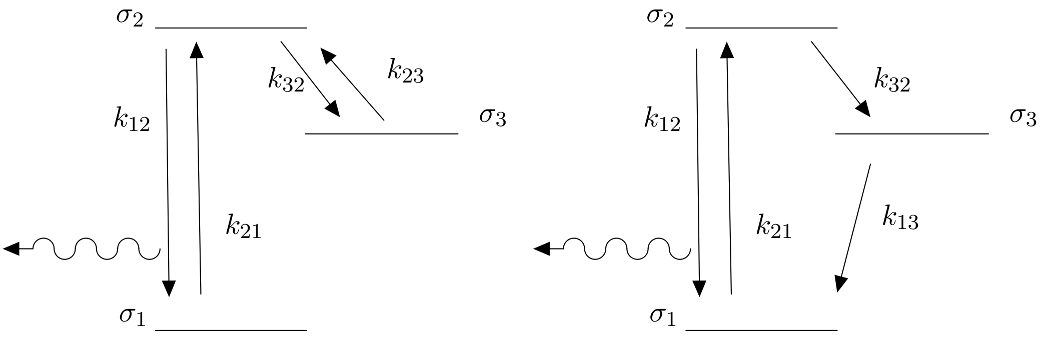

(a) **(b)**

Figure 1.4: (a) Three-level system model considered in ref. [20] and (b) three-level system model describing the dynamics of NV centers. The generation of photons occurs during the radiative decay from the first excited state (level 2) to the ground state (level 1). The shelving state (level 3) is responsible for the additional bunching feature around $\tau = 0$.

ground state, except when a photon has just been emitted. After emitting a first photon the system will be certainly in its ground state (level 1), thus generating a minimum in the second photon emission probability (antibunching dip). The next visited level must be the first excited, so that a maximum of the conditioned emission probability is recorded before stationary probability distribution between the three levels is reached.

The three-level system model considered by Beveratos et al. [20] is shown in figure 1.4a, where k_{ij} is the transition rate from state j to state i, and σ_i the population of state i. The emission probability of the system, conditioned to a first radiative decay to the ground state at time zero, is found by solving the rate equations 1.8 for the populations with initial conditions 1.9. In fact, $g^{(2)}(\tau > 0)$ is proportional to such conditioned emission probability, which in turn is proportional to the population of level 2 at time τ (see equation 1.10).

$$\begin{aligned}
\frac{\mathrm{d}\sigma_1(t)}{\mathrm{d}t} &= -k_{21}\sigma_1(t) + k_{12}\sigma_2(t) \\
\frac{\mathrm{d}\sigma_2(t)}{\mathrm{d}t} &= k_{21}\sigma_1(t) - k_{12}\sigma_2(t) - k_{32}\sigma_2(t) + k_{23}\sigma_3(t) \\
\frac{\mathrm{d}\sigma_3(t)}{\mathrm{d}t} &= k_{32}\sigma_2(t) - k_{23}\sigma_3(t)
\end{aligned} \tag{1.8}$$

$$\sigma_1(0) = 1 \qquad \sigma_2(0) = 0 \qquad \sigma_3(0) = 0 \tag{1.9}$$

The previous equations are solved by Wolfram's Mathematica for $\tau > 0$. The solution is in the form

$$g^{(2)}(\tau) = \frac{\sigma_2(\mid \tau \mid)}{\sigma_2(\infty)} = 1 - Ae^{-a|\tau|} + Be^{-b|\tau|} \tag{1.10}$$

where A, a, B, and b are functions of the transition rates k_{ij}. Considering $k_{ij} > 0 \quad \forall i, j$, it can be shown that $A > 0 \wedge 1 - A + B = 0 \wedge a > b > 0$; moreover, if $k_{23} < k_{21}$, as is the case with a long lived shelving level, $B > 0$. As a result $-Ae^{-a|\tau|}$ represents a relatively narrow antibunching dip, whereas $Be^{-b|\tau|}$ describes a broader bunching peak. Finally, it is possible to relate the lifetime of level 2 to the width of the antibunching dip:

$$\begin{aligned}
a(k_{21}, k_{12}, k_{32}, k_{23}) &= \frac{1}{2}\left[k_{21} + k_{12} + k_{32} + k_{23} + \right. \qquad (1.11)\\
&\left. + \sqrt{(k_{21} + k_{12} + k_{32} + k_{23})^2 - 4(k_{21}k_{32} + k_{21}k_{23} + k_{12}k_{23})}\right]\\
b(k_{21}, k_{12}, k_{32}, k_{23}) &= \frac{1}{2}\left[k_{21} + k_{12} + k_{32} + k_{23} + \right. \qquad (1.12)\\
&\left. - \sqrt{(k_{21} + k_{12} + k_{32} + k_{23})^2 - 4(k_{21}k_{32} + k_{21}k_{23} + k_{12}k_{23})}\right]
\end{aligned}$$

$$\lim_{\substack{k_{21} \to 0 \\ k_{23} \to 0}} a(k_{21}, k_{12}, k_{32}, k_{23}) = k_{12} + k_{32} = 1/\tau_2 \tag{1.13}$$

$$\lim_{\substack{k_{21} \to 0 \\ k_{23} \to 0}} b(k_{21}, k_{12}, k_{32}, k_{23}) = 0 \tag{1.14}$$

This means that at vanishing pump power and with a long lived level 3, $1/a$ approaches the lifetime of level 2. In the opposite case, as the dynamics gets faster (mainly because of fast pumping from level 1 to level 2) the antibunching feature in $g^{(2)}(\tau)$ becomes narrower around $\tau = 0$.

For an accurate description of the NV centre dynamics Beveratos model should be slightly modified by allowing level 3 to decay to level 1 instead of going back to level 2 (see figure 1.4b). The modified rate equations 1.15 should then be solved with the same initial conditions 1.9.

$$\begin{aligned}
\frac{\mathrm{d}\sigma_1(t)}{\mathrm{d}t} &= -k_{21}\sigma_1(t) + k_{12}\sigma_2(t) + k_{13}\sigma_3(t)\\
\frac{\mathrm{d}\sigma_2(t)}{\mathrm{d}t} &= k_{21}\sigma_1(t) - k_{12}\sigma_2(t) - k_{32}\sigma_2(t) \qquad (1.15)\\
\frac{\mathrm{d}\sigma_3(t)}{\mathrm{d}t} &= k_{32}\sigma_2(t) - k_{13}\sigma_3(t)
\end{aligned}$$

The solution for $\sigma_2(t)$ has the same form as in Beveratos model (see equation 1.10), with $a > b > 0$ and $1 - A + B = 0$. Once more, $A, B > 0$ provided that the shelving

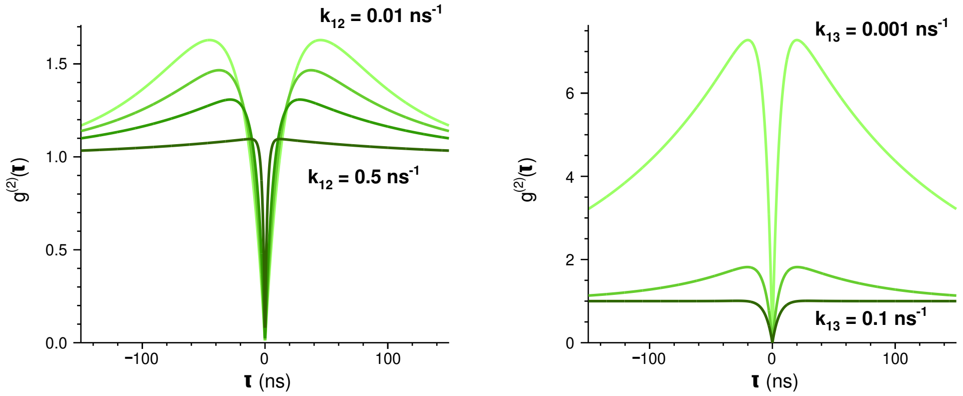

(a) $k_{12} = 0.01, 0.04, 0.1, 0.5\,\mathrm{ns}^{-1}$ ($k_{21} = 0.04\,\mathrm{ns}^{-1}$, $k_{32} = 0.01\,\mathrm{ns}^{-1}$, $k_{13} = 0.007\,\mathrm{ns}^{-1}$)

(b) $k_{13} = 0.001, 0.007, 0.1\,\mathrm{ns}^{-1}$ ($k_{12} = 0.04\,\mathrm{ns}^{-1}$, $k_{32} = 0.01\,\mathrm{ns}^{-1}$, $k_{21} = 0.12\,\mathrm{ns}^{-1}$)

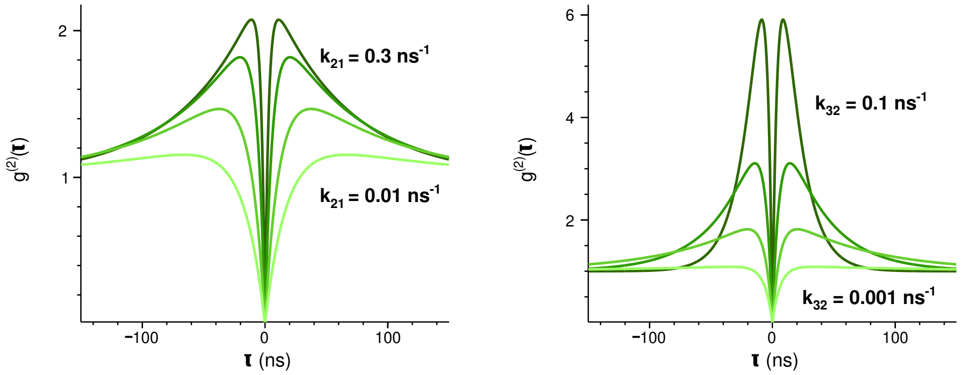

(c) $k_{21} = 0.01, 0.04, 0.12, 0.3\,\mathrm{ns}^{-1}$ ($k_{12} = 0.04\,\mathrm{ns}^{-1}$, $k_{32} = 0.01\,\mathrm{ns}^{-1}$, $k_{13} = 0.007\,\mathrm{ns}^{-1}$)

(d) $k_{32} = 0.001, 0.01, 0.03, 0.1\,\mathrm{ns}^{-1}$ ($k_{12} = 0.04\,\mathrm{ns}^{-1}$, $k_{21} = 0.12\,\mathrm{ns}^{-1}$, $k_{13} = 0.007\,\mathrm{ns}^{-1}$)

Figure 1.5: Second order correlation function according to the three-level system model for NV centers (see equations 1.15). The effect of the following transition rates is shown: (a) radiative decay rate from first excited level, k_{12} (b) decay rate from shelving level, k_{13} (c) pump rate to first excited level and, k_{21} (d) transition rate towards shelving level, k_{32}. Darker curves correspond to faster transitions.

level lifetime is long enough (precisely $k_{13} < k_{12} + k_{21} + k_{32} - 2\sqrt{k_{32}k_{21}}$). The previously found relation between a and the lifetime τ_2 at vanishing pump power is unaffected by the modification of rate equations:

$$\begin{aligned} a(k_{21}, k_{12}, k_{32}, k_{13}) &= k_{21} + k_{12} + k_{32} + k_{13} + \\ &+\sqrt{(k_{21} + k_{12} + k_{32} + k_{13})^2 - 4(k_{21}k_{32} + k_{21}k_{13} + k_{12}k_{13} + k_{32}k_{13})} \end{aligned} \tag{1.16}$$

$$\begin{aligned} b(k_{21}, k_{12}, k_{32}, k_{13}) &= k_{21} + k_{12} + k_{32} + k_{13} + \\ &-\sqrt{(k_{21} + k_{12} + k_{32} + k_{13})^2 - 4(k_{21}k_{32} + k_{21}k_{13} + k_{12}k_{13} + k_{32}k_{13})} \end{aligned} \tag{1.17}$$

$$\lim_{\substack{k_{21} \to 0 \\ k_{13} \to 0}} a(k_{21}, k_{12}, k_{32}, k_{13}) = k_{12} + k_{32} = 1/\tau_2 \tag{1.18}$$

$$\lim_{\substack{k_{21} \to 0 \\ k_{13} \to 0}} b(k_{21}, k_{12}, k_{32}, k_{13}) = 0 \tag{1.19}$$

In figure 1.5 the dependence of the single center $g^{(2)}(\tau)$ on the four transition rates is shown. In particular, a faster dynamics between levels 1 and 2 produces a narrower antibunching dip, which is reasonable: the faster the exit from ground state, the closer in time the two photons of a coincidence. Moreover, we can see that the bunching feature increases with the ratio k_{32}/k_{13}: indeed, if σ_2 is fixed, the occupation σ_3 of level 3 in stationary conditions is proportional to k_{32}/k_{13}; the higher σ_3, the stronger the shelving capability of state 3.

HBT and single photon purity HBT measurements are regularly used to assess the degree of Single Photon Purity (SPP) of a light source. In fact, the depth of the antibunching dip sets an upper bound to the number of emitters. Assuming that N emitters are fluorescing with the same intensity, $g^{(2)}(0) = 1 - 1/N$ should be measured, in principle, by an ideal setup. In other words, if a photon generated at time 0 is detected, the other $N - 1$ emitters can independently generate one photon at the same time; on the contrary, at times much larger than typical evolution of the system, the available emitters are again N. Consequently, the ratio of zero time to infinite time coincidence probability is $1 - 1/N$. More formally, with an N-photon Fock state, the second order correlation reads:

$$g^{(2)}(0) = \frac{\langle N|\, \hat{a}^\dagger(0)^2\, \hat{a}(0)^2\, |N\rangle}{\langle N|\, \hat{a}^\dagger(0)\, \hat{a}(0)\, |N\rangle^2} = \frac{N(N-1)}{N^2} \tag{1.20}$$

The figure of merit that is usually exploited is the Single Photon Purity, defined as SPP$= 1 - g^{(2)}(0)$. It is worth noticing that SPP > 0.5, or equivalently $g^{(2)}(0) < 0.5$, implies the presence of a single emitter, since N identical emitters would produce at most SPP $= 1/N$. Additional classical background deteriorates SPP.

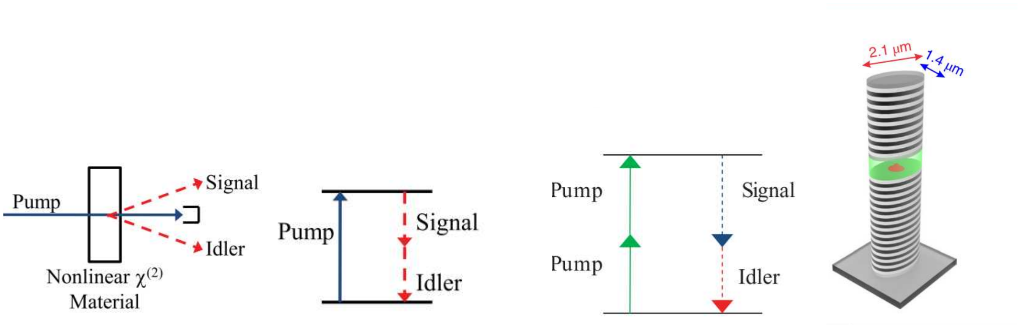

(a) **(b)** **(c)** **(d)**

Figure 1.6: (a) - (b) Scheme of a SPDC process for the generation of entangled signal-idler photons [23]. (c) Scheme of a FWM process having the same purpose [23]. (d) Representation of a Quantum Dot (QD) in cavity [24]. The top mirror (distributed bragg reflector) is made slightly less reflective in order to allow directional outcoupling of the QD emission. The cavity is ellipsoidal in order to control the polarization state of the generated photon.

1.3 State of the art

Heralded sources and spontaneous parametric down-conversion. The earliest approach to high quality single photon generation exploits the nonlinear conversion of pump photons, as schematized in figure 1.6. The most widespread technology is Spontaneous Parametric Down-Conversion (SPDC), related to the second order nonlinearity of a crystal, but the third order nonlinearity is used as well (Four Wave Mixing, FWM). Typical SPDC crystals are beta-barium borate (BBO) [12], periodically-poled potassium titanyl phosphate (PPKTP) [21], or periodically-poled lithium niobate (PPLN) [22].

The main emission from the crystal consists of pairs of entangled photons satisfying energy and momentum conservation with respect to pump photons. In order to overcome the probabilistic nature of the generation process, a heralding mechanism is exploited, consisting in the detection of one photon (idler) that “announces” the existence of its entangled counterpart (signal). More sophisticated pseudo-deterministic sources can be obtained through time multiplexing techniques [22]: a train of pump pulses is sent towards the nonlinear crystal, and the generated signal photons are stored in a variable delay line. Upon successful idler detection, the corresponding signal is adequately delayed and conveyed into the experiment, while further photons stemming from the same pulse train are blocked. Thus, deterministic manipulation compensates for the low and probabilistic generation success within a single pump pulse, at the expense of a more complex setup, which hinders scalability and speed.

The generated state is defined as spectrally factorable if it can be written as the product of two single photon states. If this is the case, the detection of the idler does not affect the signal spectrum. This is relevant because two consecutive photons with different spectra are clearly not identical. Non-factorable sources can be improved in terms of indistinguishability by spectral filtering, at the expense of source brightness; however, spectrally factorable SPDC has been experimentally demonstrated, achieving a high degree of indistinguishability [21]. While SPDC can produce high quality photons (SPP ~ 1, HOMV ~ 1) with no need for vacuum or cryogenic cooling, low pumping intensities are generally chosen to suppress multiphoton components, so that simultaneous achievement of high brightness and single photon purity is rather demanding in terms of resources, such as multiplexing equipment.

Quantum Dots The second major technology consists of Quantum Dots (QD). The transition from excited to ground state of a single QD is exploited to generate single photons with optimal SPP. The QD is prepared in its excited state through pulsed excitation, and spontaneous emission is collected. Scattered pump light is eliminated either by means of cross polarization or non resonant excitation with subsequent spectral filtering [14]. Contrary to SPDC, a QD can be excited and generate a photon exactly once per laser pulse with success probability close to 1. Optimal sources were recently obtained by coupling the QD to a planar or plano-concave cavity and by exploiting electrical polarization to stabilize the QD charge and reduce the noise that is detrimental to indistinguishability [14, 25, 26]. A further benefit of cavity coupling is the shortening of the lifetime, which makes it possible to increase the repetition rate, and thus the overall speed of the source. Latest implementations reach 1GHz repetition rate [26]. Moreover, cavities with polarization dependent resonance [24] or two color resonant excitation [27] allow to coherently drive the QD to its excited state, with the emission decoupled from excitation. Such solutions help to increase the source brightness.

The major drawback of QDs lies in the need for cryogenic cooling. However, recent efforts led to the demonstration of room temperature-operated devices with outstanding SPP and brightness [28–31]. Unfortunately, due to high dephasing, the achievement of indistinguishability at room temperature remains a challenging task [32].

Other single photon emitters Molecules, single ions, or solid state qbits can also be exploited to produce single photons, as they sometimes offer good room temperature emission properties. Similarly to QD, single photon emission per pulse can be made to occur with probability close to 1. However, the emitter trapping and manipulation can be non trivial in the case of molecules and ions. Moreover, such systems often exhibit luminescence instability, referred to as photobleaching and photoblinking [23].

Cavity coupling Nowadays, all single photon sources based on single emitters exploit cavity enhancement. The idea is to hugely increase the optical density of states of a single mode in resonance to a transition of the system, in order to increase the corresponding spontaneous decay rate (so called Purcell enhancement, or weak coupling). A cavity can address several issues:

- emission occurs preferentially in the cavity spatial mode, so that collection efficiency is greatly enhanced;
- the selectivity of cavity coupling results in the suppression of unwanted radiative transitions (such as phonon sidebands in NV centers, described in chapter 2), while maintaining only the most suitable one. Furthermore, the spectral narrowing solves the problem of inhomogeneous line broadening, allowing a lifetime-limited emission linewidth, which is sought primarily in quantum processing applications in order to achieve indistinguishability, and so quantum interference;
- the lifetime is reduced and the repetition rate of the source can be consequently increased.

Several cavity designs are used, among which the most popular is the plano-concave cavity, owing to its overall flexibility [33, 34] (see figure 1.7a). In fact, one of the mirrors can be moved with nanometric precision, which means that a scanning of the sample deposited on the movable mirror can be performed, until the optimal emitter can be found. The distance between the mirrors can be then adjusted so that the cavity mode is made resonant to the desired transition. The volume of the cavity is kept as small as possible – usually limited by dust grains which prevent the mirrors from getting closer – since this results in a higher Purcell factor[1].

Another approch consists in fabricating a defect inside a photonic crystal in dielectrics. The defect should support an optical mode lying in the bangap of the crystal, so that localization (volume confinement) occurs. Once more, the confinement yields an increase in the density of optical states in a specific mode, potentially speeding up spontaneous decay. This method is mainly used when spectral tuning is not needed (such as for phonon sideband amplification), and requires a precise nanopositioning of the emitter [35]. However, interesting results can be obtained with precise deterministic fabrication (i.e., electron beam lithography): volume confinement can reach outstanding levels by simultaneously exploiting the photonic cavity and the field hotspots between sharp edges of nanostrutures [36, 37] (see figures 1.7b–1.7d). The volume reduction is advantageous for allowing low quality factor cavities to have high Purcell enhancement. In turn, low quality factor is related to broad band amplification, which is desirable for room temperature NV Zero Phonon Line (ZPL) coupling, for example.

---

[1] The Purcell factor is the ratio of the decay rate into the cavity mode to the decay rate into all other modes in vacuum. Ultimately, it evaluates the enhancement of optical states and the consequent decay rate enhancement. It is directly proportional to the cavity quality factor and inversely proportional to the mode volume: $P \propto Q/V$.

Further solutions, such as ring, disk nanoresonators and waveguides are successfully applied to the emission enhancement of single quantum systems [38] (see figure 1.7e). This is usually the case with integrated circuits. Again, fine spectral tuning is possible, but not easy.

Besides cavities, fluorescence collection can be increased through collimating devices such as nanolenses and scattering gratings [39, 40] (see figure 1.7f). These structures are often used with NV centers because of an intrinsic collection problem at the surface of diamond films: The refractive index in bulk diamond ($n \sim 2.4$) is much higher than in air. As a result, total internal reflection prevents most of the emitted photons from exiting the sample. This is one of the reasons why nanodiamonds smaller than 100 nm are often chosen instead of bulk samples: in this case the effective refractive index seen by the defect is close to that of air, eliminating the surface loss due to internal reflection.

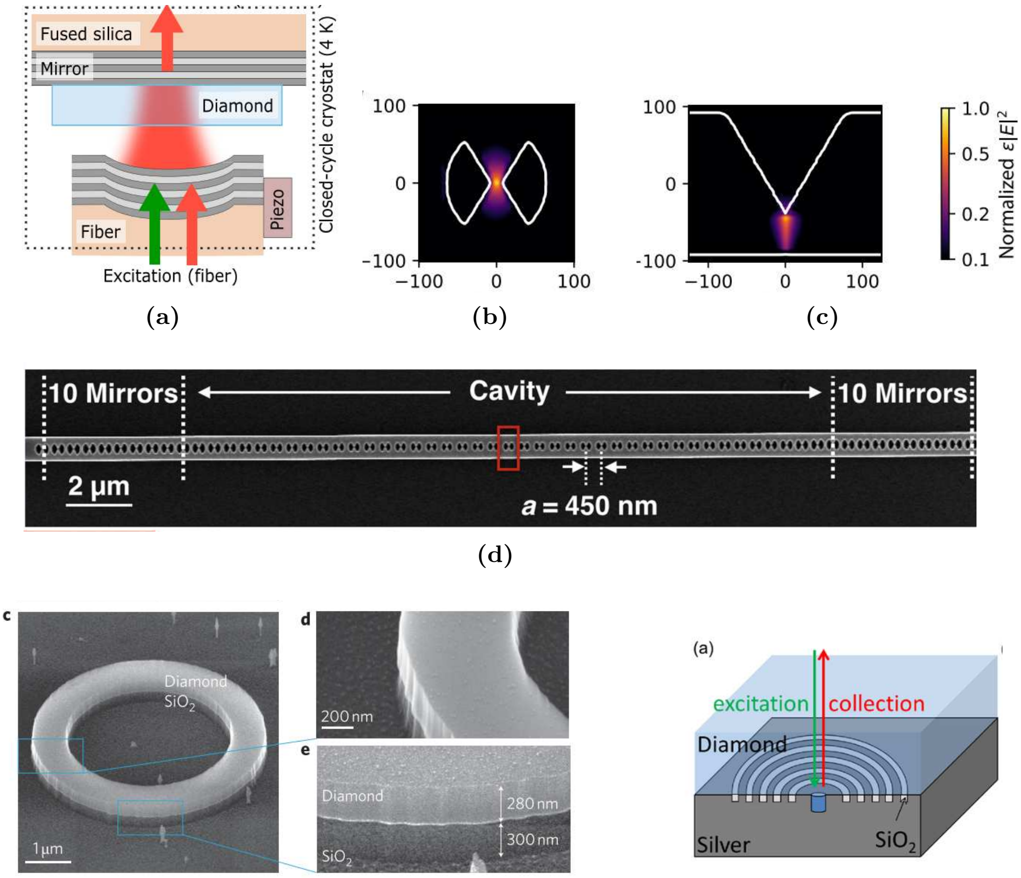
Fused silica
Mirror
Diamond
Fiber
Piezo
Closed-cycle cryostat (4 K)
Excitation (fiber)
100
0
−100
−100
0
100
100
0
-100
−100
0
100
1.0
0.5
0.2
0.1
Normalized $\epsilon|E|^2$
10 Mirrors
Cavity
10 Mirrors
2 µm
$a = 450$ nm
c
Diamond
SiO$_2$
1µm
d
200 nm
e
Diamond
280 nm
300 nm
SiO$_2$
(a)
excitation
collection
Diamond
Silver
SiO$_2$

(a) (b) (c)

(d)

(e) (f)

Figure 1.7: (a) Plano-concave cavity made of two distributed Bragg reflectors [34]. The resonance frequency is adjustable thanks to the nanopositioners. Representation of the (b) x-y and (c) y-z profiles of a photonic lattice unit cell (spatial coordinates expressed in nm) [37]. The simulated field intensity is shown in order to highlight the mode confinement in the field hotspot of the bow-tie structure. The corresponding photonic cavity is shown in (d), and consists of a defect in a 1-D photonic crystal [36]. The cavity is built by modulating the dimensions of the unit cell, and supports a mode whose frequency lies in the bangap of the photonic crystal (mirrors). (e) Ring cavity for the Zero Phonon Line (ZPL) enhancement [38]. (f) Circular collection grating with the purpose of scattering the emission towards the detectors [40].

Chapter 2

Nitrogen-Vacancy centers in diamond

Nitrogen-Vacancy (NV) centers are defects in diamond consisting of a substitutional nitrogen atom next to an empty lattice site, as shown in figure 2.1. They have been extensively studied since the middle of the last century; one of the reasons is the presence of electronic levels in the middle of the diamond bandgap (whose width is 5.5 eV) that do not interfere with the continuum of the band levels. Consequently, as far as the interaction with light is concerned, they behave like isolated molecules, with the advantage of an easier mechanical manipulation due to the presence of either bulk or nanostructured diamond around it. Radiative transitions between localized electronic levels of NV centers result in a characteristic photoluminescence, hence the name “color centers”.

The attractiveness of NV centers for single photon emission lies in the remarkable room temperature emission properties, among which the photostability must be cited. Indeed, the photobleaching of NV centers is relatively low under most operating conditions. Overall they are a viable alternative to quantum dots, in particular for quantum cryptography applications, as already shown by Beveratos [11].

In this chapter the main electronic, phononic, and emission properties of NV centers are presented, along with their usefulness for NV identification, nanosensing and quantum information. Moreover, a brief summary of the synthesis techniques and the related problems is reported.

2.1 Electronic levels

As anticipated at the beginning of the chapter, the NV center [41] consists of a substitutional nitrogen atom next to a vacancy in the diamond lattice. In a neutral center, the three carbon atoms around the vacancy have three dangling bonds, with one electron each; on the other hand, the nitrogen atom has a two electron dangling

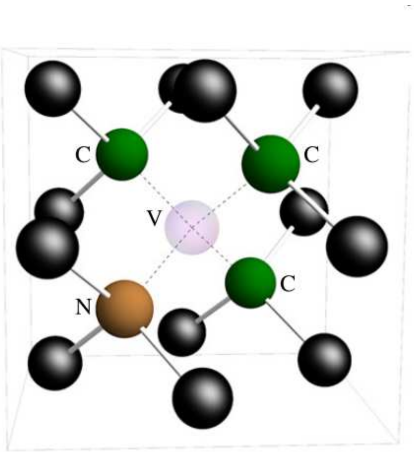

Figure 2.1: Atomic model of the Nitrogen-Vacancy (NV) center in diamond [41]. Black spheres represent carbon atoms in a diamond lattice. Carbon atoms adjacent to the vacancy are highlighted in green.

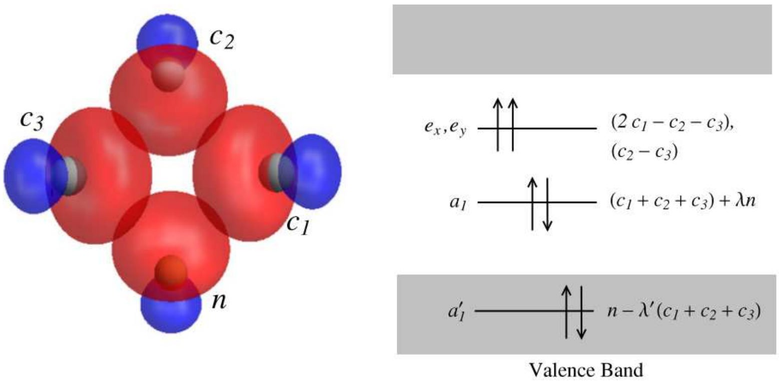
c_2
c_3
c_1
n
e_x, e_y
$(2c_1 - c_2 - c_3)$,
$(c_2 - c_3)$
a_1
$(c_1 + c_2 + c_3) + \lambda n$
a'_1
$n - \lambda'(c_1 + c_2 + c_3)$
Valence Band

Figure 2.2: Left: spatial representation of the atomic orbitals (dangling bonds) of the three carbon atoms adjacent to the vacancy and the nitrogen atom. Right: molecular orbitals of the defect, written as linear combinations of the atomic orbitals shown on the left [41].

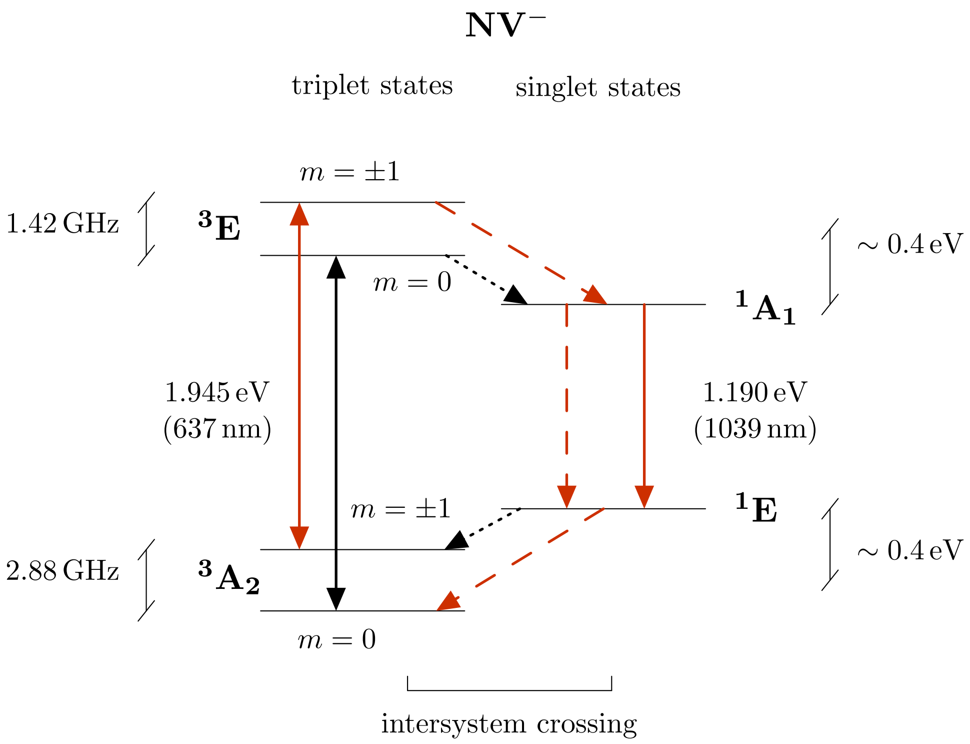
NV⁻
triplet states
singlet states
m = ±1
³E
m = 0
1.42 GHz
¹A₁
~ 0.4 eV
1.945 eV
(637 nm)
1.190 eV
(1039 nm)
m = ±1
¹E
~ 0.4 eV
2.88 GHz
³A₂
m = 0
intersystem crossing

Figure 2.3: Room temperature electronic levels of the negatively charged state of the NV center. Solid lines represent radiative transitions, dashed lines phonon mediated strong transitions, and dotted lines phonon mediated weak transitions. The optical spin polarization cycle is highlighted in red. Only Zero Phonon Lines (ZPL) are considered in the scheme. All the transitions that are not marked with an arrow (such as $^1A_1 \rightarrow {}^3A_2$, $^3E \rightarrow {}^1E$, or between spin sublevels of the triplet states) are orders of magnitude slower than the marked ones [41].

bond extending toward the same empty lattice site. At first, the electronic states can be pictured as the linear combinations of these “dangling orbitals”, as shown in figure 2.2. Such states are occupied by 5 electrons in a neutral center, or 6 in a negatively charged one. More frequently, the multiple-electron state of the defect is summarized into a unified level scheme (see figure 2.3) as long as valence- or conduction-band charge carriers do not take part in the dynamics, that is, unless ionization occurs.

The levels are named after the irreducible representations of the defect symmetry group [41]. The NV center is invariant under $\pm 2\pi/3$ rotations around the N-V axis, and under symmetry with respect to “vertical” planes, namely, planes containing the symmetry axis and one of the carbon atoms adjacent to the vacancy. The group of such transformations is named C_{3v}, and its three irreducible representations are:

- A_1, whose elements are invariant under all transformations of the C_{3v} group;
- A_2, whose elements are invariant under $2\pi/3$ rotations;
- E, whose element are not invariant for any C_{3v} transformation;

Consequently, under a C_{3v} symmetry transformation, an orbital will behave as the elements of the irreducible representation from which it borrows the name.

Let’s consider now the negatively charged NV^- center [41], which is usually the most abundant: in the ground state $^3\mathrm{A}_2$, the two parallel spin electrons occupying the e_x and e_y orbitals form a spin triplet. Since radiative transitions do not promote spin flip, the first excited state $^3\mathrm{E}$, which is optically coupled to the ground state, will be a triplet as well. Two singlet states, that is $^1\mathrm{A}_1$ and $^1\mathrm{E}$, lie approximately in the middle between $^3\mathrm{A}_2$ and $^3\mathrm{E}$; the spin flip transition (i.e., between triplet and singlet states) is called inter-system crossing and is mediated by phonons. The interesting feature about inter-system crossing is that its rate depends on the spin projection of the triplet. Indeed, the transition rate $^3\mathrm{E}(m = \pm 1) \to {}^1\mathrm{A}_1$ is of the same order of magnitude as the decay rate to the ground state $^3\mathrm{E} \to {}^3\mathrm{A}_2$, but significantly higher than the corresponding transition rate from the zero spin projection level $^3\mathrm{E}(m = 0) \to {}^1\mathrm{A}_1$. The phenomenon is sometimes referred to as quenching, since the radiative yeld from $m = \pm 1$ spin projections is reduced by a competing non radiative process. Similarily, the intersystem crossing to the zero spin ground state $^1\mathrm{E} \to {}^3\mathrm{A}_2(m = 0)$ is faster than its non-zero ($m = \pm 1$) counterpart. Such spin selectivity is a great advantage in terms of spin manipulation and spectroscopy techniques, as will be explained below.

In table 2.1 the average room temperature lifetimes of the NV^- levels are reported for bulk diamond and nanodiamonds (NDs). Nonetheless, the broad lifetime distribution of the excited state $^3\mathrm{E}$ in single NV^- centers in NDs should be considered (see figure 2.4a). This is probably due to the variety of center orientations and positions with respect to the surface and neighbouring defects, which may favour or hinder competing non radiative decays. Notice that the substrate (a coverslip

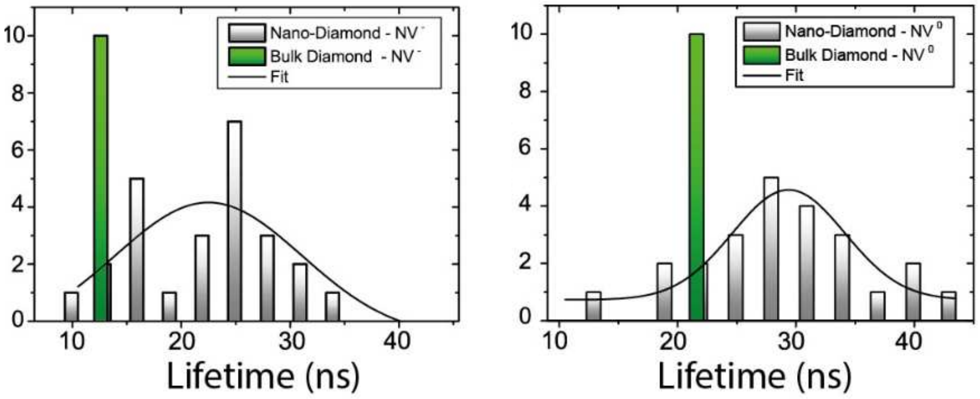

(a) (b)

Figure 2.4: Single center lifetime histograms for (a) NV^- and (b) NV^0 [43]. The green column points out the lifetime of the first excited state in bulk diamond, whereas the broad distribution represents the lifetime of the first excited state of single centers in nanodiamonds. The centers are excited at 540 nm, while fluorescence is collected at $700\,\text{nm} < \lambda < 800\,\text{nm}$ for NV^- and at $600\,\text{nm} < \lambda < 650\,\text{nm}$ for NV^0. With NV^-, no distinction is made between the fluorescence of the different spin sublevels of ^3E. However, given the high repetition rate (1 MHz) it is possible that partial spin polarization into $m = 0$ is occurring.

in the case of figure 2.4) also affects the lifetime of NV centers in NDs: if NDs are suspended in a gel with refractive index $n \sim 1$ instead of being deposited on a coverslip, the average lifetime of ^3E increases from $\tau \approx 23\,\text{ns}$ to $\tau \approx 31\,\text{ns}$ [42].

Spin relaxation and coherence Spin relaxation time T_1 is the decay time of a spin-polarized state of the center, namely the average time necessary for the spin population to re-distribute among the three sublevels. On the contrary, spin coherence time T_2 is the typical survival time of a quantum superposition of spin states. Both T_1 and T_2 are crucial figures of merit that need to be much larger than typical processing times in quantum information. According to Doherty et al. [41], at room temperature the typical spin relaxation time is in the order of $T_1 \sim 10\,\text{ms}$ and the typical coherence time $T_2 \sim 1\,\mu\text{s}$. However, in isotopically pure diamond coherence exceeds 1 ms because the perturbation due to neighbouring nuclear spins is reduced to a minimum. While relaxation mainly occurs via a two phonon process (with energy $\sim 67\,\text{meV}$ each), decoherence is governed by the interaction with the nuclear spin of ^{14}N, of the neighbouring ^{13}C and ^{14}N atoms, and the electronic spins of the neighbouring color centers. As a result T_1 can be improved by cooling the system, whereas an enhancement in T_2 requires considerable diamond purification.

Level	τ (ns)	temperature	substrate	notes
^{3}E$(m = 0)$	12.0	room	bulk	Batalov [44]
^{3}E$(m = 0)$	13.7	room	bulk	Robledo [45]
^{3}E$(m = \pm 1)$	7.8	room	bulk	Batalov [44]
^{3}E$(m = \pm 1)$	7.3	room	bulk	Robledo [45]
^{3}E$(m = 0)$	23	room	ND	Neumann [46]
^{3}E$(m = 0, \pm 1)$	25	room	ND	Beveratos [47]
^{3}E$(m = \pm 1)$	12.7	room	ND	Neumann [46]
^{1}A$_1$	0.9	$4 \div 70\,$K	bulk	Acosta [48]
^{1}E	460	$4 \div 70\,$K	bulk*	Acosta [48]
^{1}E	370	$< 5\,$K	bulk*	Robledo [45]
^{1}E	170	room	bulk*	Robledo [45]

Table 2.1: Lifetimes of the electronic levels of the NV$^-$ center [41]. When considering nanodiamonds (ND) the change in the refractive index has a visible effect in the lifetime of the excited state ^{3}E. The true shelving level is the lower energy singlet state ^{1}E.

* The decay from ^{1}E is not radiative, as a result the refractive index of the environment should not be relevant.

Room temperature fine structure The fine structure splitting that can be seen in figures 2.5a and 2.3 is mainly due to spin-spin coupling, while spin-orbit coupling carries second order contributions only [41]. It should be stressed that the splitting between $m = 0$ and $m = \pm 1$ spin projections occurs in absence of magnetic fields, and can be detected at room temperature, despite a much lower energy than thermal phonons. In fact, the optical and phononic coupling between different spin projections is negligible, as a first approximation.

Both the ground state ^{3}A$_2$ and the excited state ^{3}E experience the zero field splitting, at the energies of 2.88 GHz and 1.42 GHz, respectively. These features are experimentally accessible through zero field magnetic resonance (see figure 2.9), as described below; their presence is the clear fingerprint of the NV$^-$ center, and provides an easy identification procedure.

Room temperature hyperfine structure due to the interaction with the nitrogen nuclear spin $I(^{14}\mathrm{N}) = 1$ can be observed as well. In figure 2.5a a scheme of the ground state hyperfine structure is reported. The excited state ^{3}E has identical room temperature hyperfine structure but different splitting values [41].

Cryogenic temperature fine structure As the system is cooled down to cryogenic temperature, the excited state fine structure becomes more complex (see figure 2.5b).

In general, the low temperature fine structure is observed in single centers be-

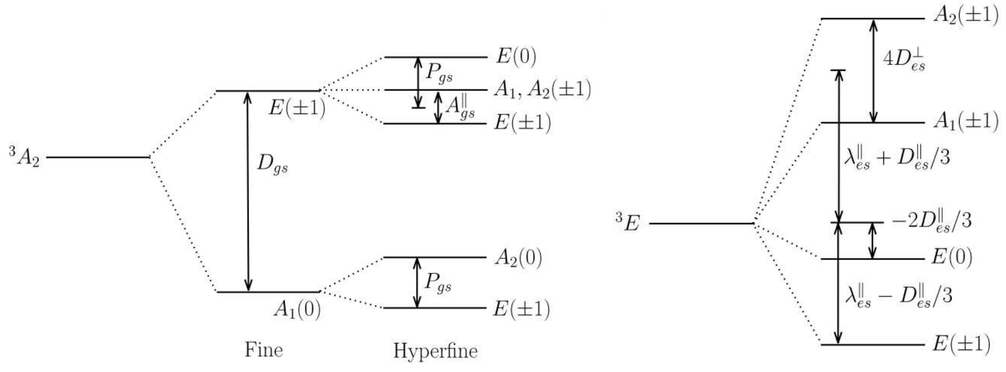

(a) **(b)**

Figure 2.5: (a) Room temperature fine and hyperfine structure of the NV$^-$ ground state [41]. The first excited state ^{3}E has equal room temperature fine and hyperfine structure, with different values for the splitting parameters. (b) Cryogenic temperature fine structure of the NV$^-$ triplet excited state (^{3}E [41]).

cause of the large inhomogeneous broadening occurring in NV ensembles. Such broadening can be ascribed to the local strain of the crystal or local fields near charged defects, that slightly modify each center's transition frequecy.

When the temperature increases, phonons promote transitions between equal-spin projection fine levels [41]. At room temperature these transitions are much faster than the other electronic dynamics, so that equal spin sublevels undergo an averaging process. Thus the room temperature fine structure can be recovered. Besides averaging between sublevels, the fast phonon transitions cause a considerable homogeneous spectral broadening ($\propto T^5$) of the whole level, that is in the order of 1 nm at room temperature (see figure 2.6).

Strain and field splitting A remarkable feature of the NV$^-$ center is the sensitivity to local strain and fields. Indeed, magnetic and electric fields, as well as crystal strain produce a splitting of the excited state sublevels into two branches; the higher the field or strain strength, the larger the splitting (see figure 2.7). This makes the center extremely appealing as a nanoscale sensor. Of course, the system must be optimized for sensing a specific quantity, since the effects of electromagnetic fields, strain, but also temperature, are similar in its spectrum.

When developing a NV based sensor, special care should be taken so that the centers are as close to the diamond surface as possible, without affecting overall stability properties. Spatial resolution and sensitivity can be thus enhanced. High density ensembles are usually exploited in these circumstances.

In other applications, a single center can detect and be made to interact with a proximal ^{13}C nuclear spin.

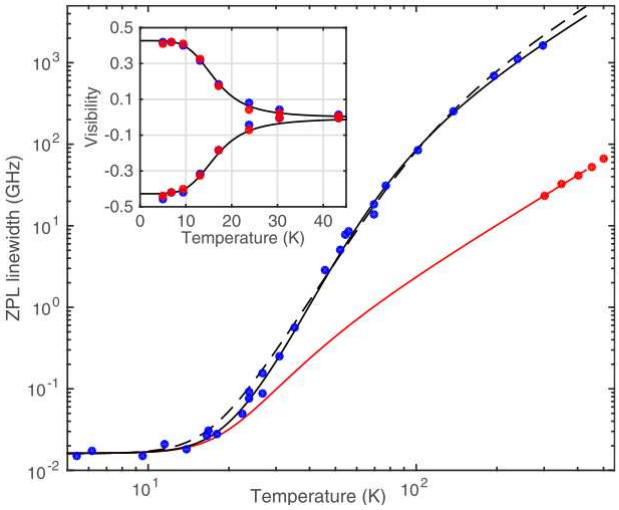

Figure 2.6: NV^{-} ZPL width as a function of temperature (blue points). Inset: polarization visibility of the ZPL of single NV^{-} centers as a function of temperature [49].

Optical spin polarization The radiative transition between the ground state ^{3}A$_{2}$ and the first excited state ^{3}E is always spin conserving, even if the final state is vibronic. This means that the main mechanism allowing to switch spin projection between $m = 0$ and $m = \pm 1$ involves inter-system crossing. And indeed, by following the fastest transition from excited state ^{3}E to ground state ^{3}A$_{2}$ through singlet states, the spin projection changes from $m = \pm 1$ to $m = 0$. If optical excitation $^{3}\mathrm{A}_{2} \rightarrow {}^{3}\mathrm{E}$ is also taken into account, the whole process is called optical spin polarization, and is highlighted by red arrows in figure 2.3.

Optical spin polarization is a powerful tool to manipulate spins. In fact, by just turning on light excitation, the defect is initialized into the $m = 0$ sublevels of the triplet states. After the pumping beam is turned off, the relaxation time T_{1} and the coherence time T_{2}, both of which can be in the order of ms, govern the spin dynamics. This means that spin projections are considerably stable, and in addition, they are suitable for qbit implementation.

Not only initialization, but also spin readout is performed by optical means: the luminescence of the $^{3}\mathrm{E}(m = \pm 1)$ state is significantly quenched by competing non radiative inter-system crossing; as a result, after photoexcitation, the zero spin projection state looks brighter than the non zero ones until optical spin polarization occurs 2.8. Since the underlying process is the same, single stage spin readout and initialization can be exploited. Improved readout techniques involving nuclear spin coupling have been succesfully implemented [50].

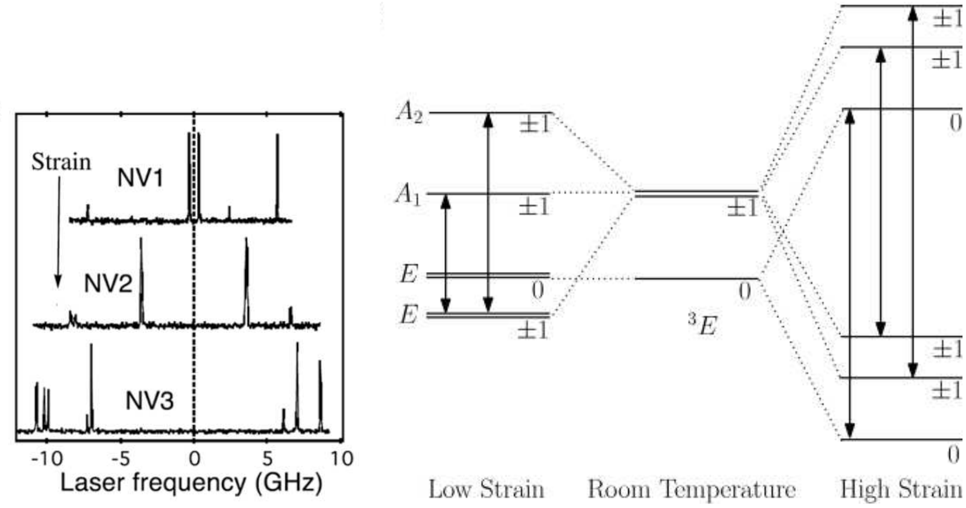

(a) **(b)**

Figure 2.7: Low temperature NV$^-$ fine structure splitting due to strain [41]. (a) Excitation spectra of NV centers with different strain. (b) Scheme of the low temperature strain splitting of ^{3}E. Similar splittings are caused by magnetic and electric fields; temperature also affects the fine structure of NV$^-$ center. The black arrows point out the phonon averaging processes between equal spin sublevels that result in the room temperature fine structure.

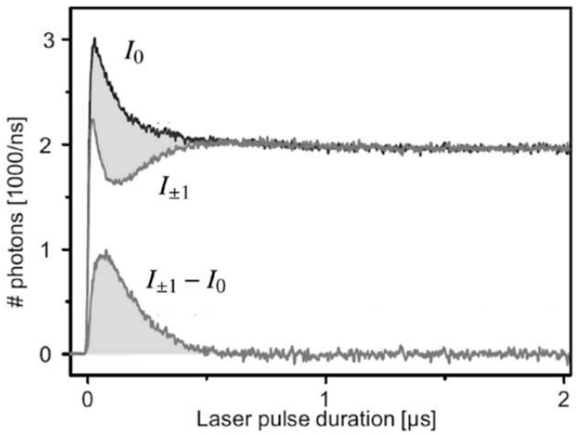

Figure 2.8: Optical spin readout in single NV$^-$ centers [41, 50]. Due to quenching nonradiative processes, the ^{3}E($m = \pm 1$) $\rightarrow$ ^{3}A$_2$ radiative decay is less luminescent the ^{3}E($m = 0$) $\rightarrow$ ^{3}A$_2$ decay, and this difference is visible until spin polarization to the $m = 0$ projection is complete.

Optically Detected Magnetic Resonance The second major advantage of the spin selective inter-system crossing is the possibility to detect zero magnetic field splittings of electronic levels by fluorescence measurements [51]. The NV$^-$ center is prepared in the $m = 0$ state, and the constant pumping beam ($\lambda < 637\,\text{nm}$) is kept on during the whole measurement. Luminescence is collected from the 637 nm zero phonon line, as well as from its phonon sideband. A perturbing microwave field is switched on, and scanned in the frequency range of interest. When the perturbing field is in resonance with the spin splitting of the ground state ^{3}A$_2$ or of the excited state ^{3}E, populations are redistributed among the three spin projections. Therefore the competing non radiative decay channel (through inter-system crossing and singlet states) is stronger than for $m = 0$ spin polarized NV$^-$ centers. As a consequence, luminescence is partially quenched. The procedure is called Optically Detected Magnetic Resonance (ODMR) and eliminates the need for microwave absorption measurements, which are more troublesome due to the lower energies involved. In figure 2.9 the double dip related to spin redistribution and luminescence quenching in a typical ODMR scan can be seen.

Notice that although the detection exploits the broad line optical transition ^{3}E $\rightarrow$ ^{3}A$_2$, room temperature splittings that are much lower than the optical linewidth are detected. This is a direct consequence of spin conservation.

2.2 Vibronic coupling

Zero Phonon Lines (ZPL), that is, direct transitions between purely electronic states have been considered so far. However, as shown in figure 2.10, the equilibrium

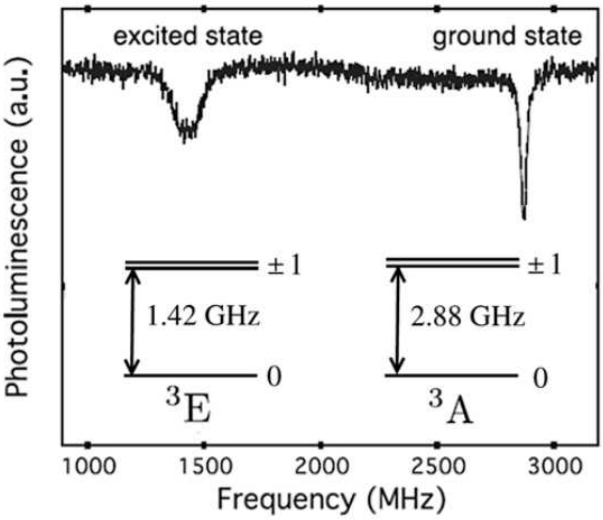

Figure 2.9: Optically Detected Magnetic Resonance (ODMR) spectrum of a NV$^-$ center [41]. When the microwave field is resonant to the spin splitting, the luminescence quenching of the $m = \pm 1$ spin projections can be seen because of the redistribution of the populations among the three spin sublevels.

configuration of nuclei in the electronic ground and first excited states are different. The inherent coupling between the electon and phonon modes makes it convenient to deal with vibronic states, that is, mixed electron and phonon states.

The ^{3}E $\leftrightarrow$ ^{3}A$_2$ transition typically ends in a mixed state, which afterwards relaxes to the pure electronic state. As a result, excitation occurs mainly at higher frequencies than ZPL, and emission at lower frequencies. The difference between maximum excitation and maximum emission frequencies is called Stokes shift, and is exploited in luminescence measurements to filter out the pumping laser beam. The broad emission and absorption spetral features beyond the ZPL (see figure 2.11) are named Phonon Side Bands (PSB). The fraction of ZPL emission to the total emission of a given electronic transition is defined as the Debye Waller (DW) factor. DW factor is really low in NV$^-$ centers even at cryogenic temperature (DW~ 0.03), and according to Gali [53], this fact suggests that 3.5 effective phonons participate in the radiative decay, on average.

In a pump-probe differential transmission experiment, Ulbricht et al. [54] report on the relaxation time to the lowest vibronic level of the excited state ^{3}E. Following selective photoexcitation from the ground state ^{3}A$_2$ to the one-phonon vibronic level of ^{3}E, the relaxation time to the zero-phonon ^{3}E state is $\tau \sim 50\,\text{fs}$. Previous work reported a relaxation time $\tau \sim 4\,\text{ps}$ upon non selective excitation of the whole ^{3}E vibronic band. In any case, vibrational relaxation is faster than electronic transitions by orders of magnitutes. One of the consequences is that the excited level can be pumped almost up to $\sigma = 1$ by non resonant ($\lambda < \lambda_{ZPL} = 637\,\text{nm}$) pulses, in

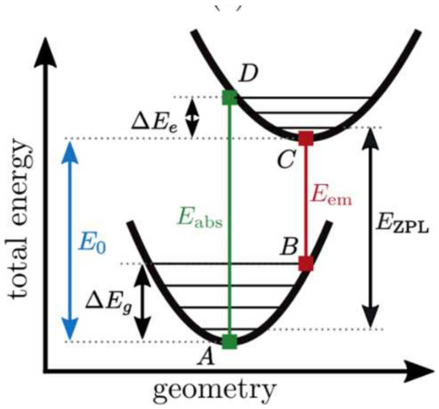
total energy
geometry
D
C
B
A
ΔE_e
ΔE_g
E_0
E_{abs}
E_{em}
E_{ZPL}

Figure 2.10: Scheme of the potential energy functions for the triplet levels of NV$^-$ and vibronic structure [52]. On the x axis, a configurational coordinate of nuclei is represented, whereas the y value corresponds to the energy of the $^3\mathrm{A}_2$ and $^3\mathrm{E}$ electronic states with fixed nuclear position (in an adiabatic approximation).

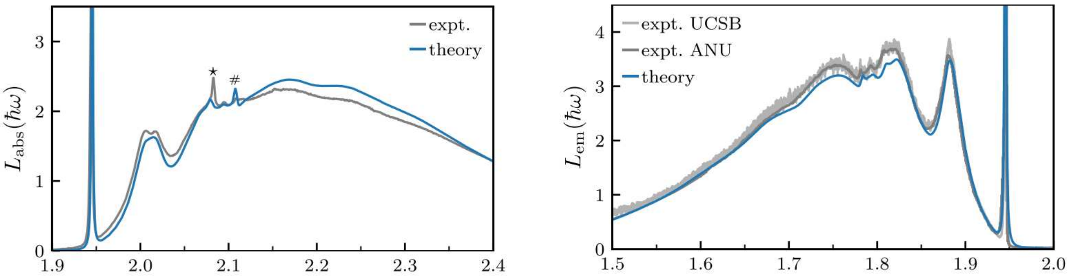

(a) **(b)**

Figure 2.11: (a) Absorption and (b) emission low temperature spectra of the NV$^-$, according to both experimental data and theoretical simulations [52]. The ZPL of the transition $^3\mathrm{E} \rightarrow {}^3\mathrm{A}_2$ can be seen at 1.945 eV (637 nm), along with its phonon sidebands.

principle.

Great effort has been devoted to the development of a model accounting for the vibronic spectra. In the first attempts, symmetric vibrations were considered [41](Huang Rhys model). It was later aknowledged, however, that modes with lower symmetry than the intrinsic C_{3v} of NV centers play a significant role in the vibronic transitions [41, 52, 53](Dynamic Jahn Teller effect). In fact, the equilibrium nuclear configuration of the excited state is not invariant under C_{3v} symmetry transformations.

In NV$^-$ the electronic levels are mainly coupled to $\sim 67\,\mathrm{meV}$ phonons, as can be seen by the spacing of phonon side band peaks. The corresponding nuclei vibration is pseudo-localized to the vacancy neighbours [41]. It can not be totally localized because the phonon band of pure diamond spans from 0 meV to 160 meV, whereas a truly localized mode would require higher frequency than any lattice vibration.

2.3 Neutral NV center and charge dynamics

As mentioned above, the most common charge state of the NV center is the negative one, but the latter can be found in the neutral charge state as well. The electronic states of NV^0 are outlined in figure 2.12. Similarily to NV$^-$, NV^0 has an optical transition $^2\mathrm{A} \leftrightarrow {}^2\mathrm{E}$ with 575 nm ZPL plus the related phonon sidebands (see figure 2.13), and $\tau({}^2\mathrm{A}) \approx 22\,\mathrm{ns}$ is the excited state lifetime in bulk [55]. The NV^0 center has been less studied than its negative counterpart, and investigations of the spin and orbit dynamics are a recent development [55].

The charge state can be controlled either by optical means, that is through photoionization, or by engineering the Fermi level. In the first case, the center is usually ionized by two-photon absorption. In fact, by pumping either NV$^-$ or NV^0 in its absorption spectral band ($\lambda \leq \lambda_{ZPL}$), charge conversion is stimulated until a stationary population is reached for the two charge states. The underlying mechanism is shown in figure 2.14 [57]. Due to the different absorption spectra of the two charge states, the steady state charge populations depend on the pump wavelength, as can be seen in figure 2.15. When NV$^-$ are selectively excited ($\lambda > 575\,\mathrm{nm}$) the effect of charge dynamics is a weakening of the luminescence in time (photobleaching); in fact, illumination induces the ionization of the center to NV^0, which is dark at such wavelengths. In addition, as the steady state is reached, the single color center undergoes continuous charge transitions between the two states, which will cause a so called luminescence blinking. After the pumping source is switched off, the NV charge in bulk samples can be stable for longer times than one week [58].

It is worth noticing that the dependence of the ionization rate on pumping power is quadratic because of the two-photon character of the process. Alternatively, it is possible to stimulate charge dynamics with single photons at higher frequencies [56].

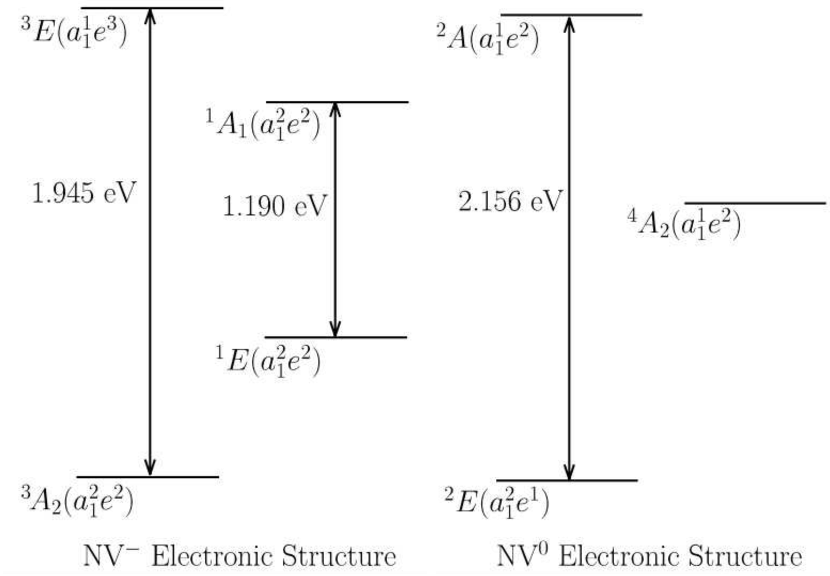

$^3E(a_1^1e^3)$
1.945 eV
$^1A_1(a_1^2e^2)$
1.190 eV
$^1E(a_1^2e^2)$
$^3A_2(a_1^2e^2)$
NV$^-$ Electronic Structure
$^2A(a_1^1e^2)$
2.156 eV
$^4A_2(a_1^1e^2)$
$^2E(a_1^2e^1)$
NV^0 Electronic Structure

(a) **(b)**

Figure 2.12: Comparison between the electronic structure of (a) NV$^-$ and (b) NV^0 [41]. The fine structure is not shown.

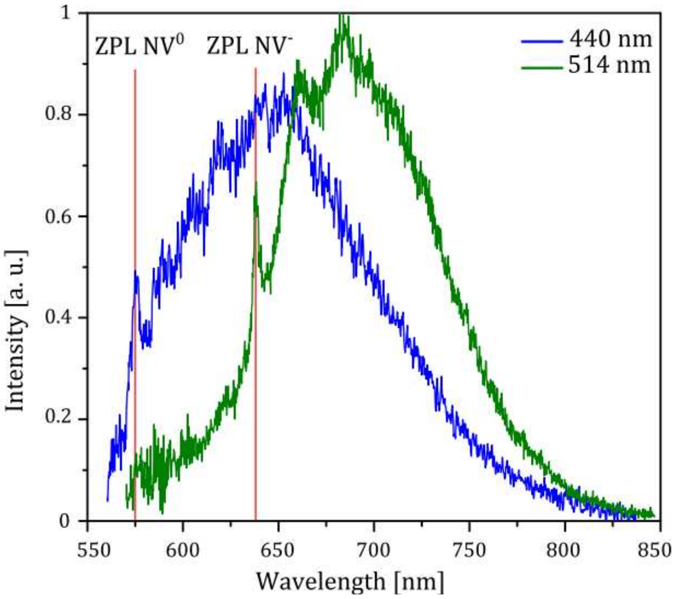

Figure 2.13: Room temperature luminescence spectra of the two charge states of the NV center [56]. Charge state selectivity is achieved by choosing the excitation wavelength (440 nm and 514 nm respectively).

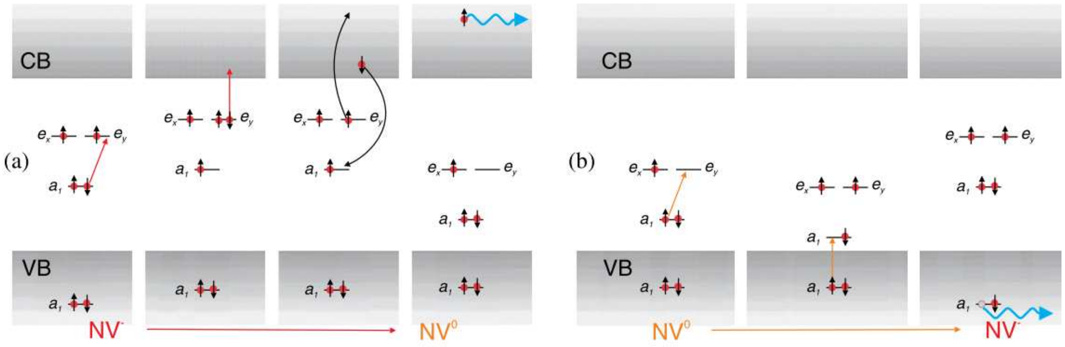

Figure 2.14: Scheme of the charge conversion process [57].

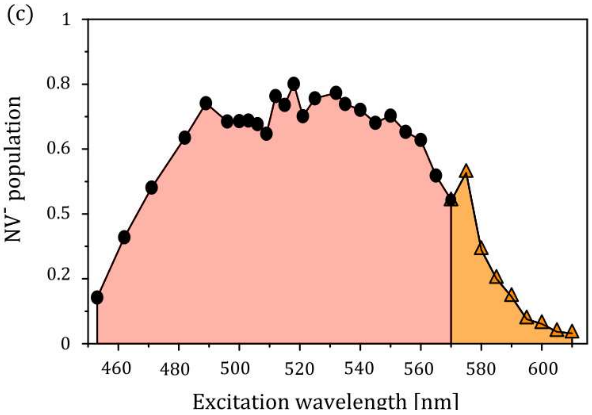

Figure 2.15: Steady state NV$^-$ population as a function of illumination wavelength [56]. For $575\,\text{nm} < \lambda \leq 637\,\text{nm}$ only NV$^-$ can be excited; as a result, charge convertion preferentially occurs toward the neutral state. On the contrary, NV^0 ZPL-resonant illumination ($\lambda = 575\,\text{nm}$) results in preferential charge conversion towards the negative state, hence the peak in the data. At $\lambda \lesssim 470\,\text{nm}$ the one-photon ionization process starts dominating.

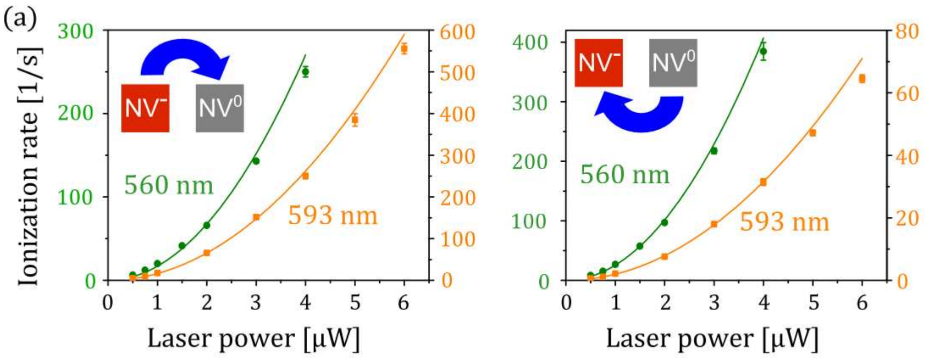

Figure 2.16: Charge conversion rate as a function of the pump power at different wavelengths [56]. The quadratic trend, due to the two-photon character of the process, is only valid in bulk diamond. Near-surface charge conversion rates show a linear dependence on pump power, and are generally higher [58].

The effect of surface proximity on the ionization rates is experimentally investigated by Dhomkar et al. [58]. The main result is that charge dynamics is faster for shallow centers ($\lesssim 10\,\mathrm{nm}$ deep) than in bulk diamond, both under illumination and dark condition. This is probably a consequence of the hybridization of NV orbitals with those of neighbouring defects, with consequent delocalization of the electron upon one-photon excitation. Indeed, the ionization rate of shallow NV centers scales linearly, and not quadratically, with the pump power; such observation supports the hypothesis of a one-photon process.

The second parameter for controlling the equilibrium charge state of the NV center is the Fermi level. This is traditionally achieved by doping in bulk crystal: in diamond , for example, native nitrogen impurities act as donors for NV centers. Once more, the diamond surface promotes different equilibrium configurations than bulk: depending on the surface termination, band bending can develop, so that in shallow centers either charge state may be favoured with respect to the other. In order to stabilize the NV^- state, a positive surface electron affinity (difference between the vacuum energy level and the bottom of the conduction band), that is downward band bending, should be sought. For example positive electron affinities can be found with oxygen surface termination, or even better, with fluorinated surface. On the contrary, hydrogen is detrimental to NV^- stability [39, 53].

2.4 NV synthesis

The main current techniques for producing synthetic (nano)diamond are High Pressure High Temperature growth (HPHT), Chemical Vapour Deposition (CVD), and detonation growth [59]. HPHT method yields the highest crystal quality diamond, which can be afterwards nanostructured in a top-down approach using electron beam lithography, reactive ion etching, and ion implantation lift off of thin films [60]. Mechanical milling of single crystal diamond is an alternative and simpler top-down nanostructuring approach, although ground fragments often have inhomogeneous size and sharp edges [59]. HPHT growth occurs in a bath of melted transition metals above 1300 °C and 5 GPa [61]. Dissolved carbon precipitates on the facet of a small seed at slightly lower temperatures. Nitrogen impurities can be then introduced in the grown crystal in a controlled fashion by ion implantation, either before or after nanostructuring.

On the other hand, CVD is exploited to epitaxially grow diamond crystals on a HPHT diamond precursor. CH_4 at about 100 mbar is degraded by microwave-induced plasma to provide carbon atoms [61]. Additional elements in the CVD atmosphere are hydrogen, which etches away the graphitic (sp_2) carbon, and in a smaller quantity, oxygen, with the purpose of reducing the amount of unwanted defects. Moreover, dopants can be directly introduced in the growth process by a controlled flux of the specified gas (typically N_2) [61], allowing a more straightforward production process.

Further single-step methods for producing fluorescent nanodiamonds are detonation growth and laser ablation. The detonation process consists in the spontaneous aggregation of carbon under localized high temperature high pressure conditions produced by an explosion. Similarily, pulsed laser ablation in liquid nitrogen was recently reported as a straightforward method to generate fluorescent nanodiamonds [62]: the laser is focused onto a graphitic target immersed in liquid nitrogen, and the ejected material directly forms fluorescent NDs, that are afterwards dispersed in water. However, because of the highly non equilibrium synthesis conditions, these methods provide little control on the localization and density of NV, and the quality of the nanocrystals, including the surface termination, which may result in unwanted short-lived ($\lesssim 1\,\mathrm{nm}$) fluorescence [63].

Nitrogen and vacancies impurities are intrinsically present, in a low concentration, in the grown diamond crystals. They can be exploited to generate NV centers by promoting vacancy migration, which can be achieved through electron beam irradiation and annealing [64]. However, nitrogen introduction by ion implantation is the standard synthesis technique, since it allows to better control the color center positioning and density. Vacancies are usually generated as a collateral damage of the implantation. After ion irradiation, annealing at about 800 °C-1100 °C is required [39, 59, 61]: by annealing, the vacancy migration towards the implanted elements is promoted, interstitial implanted ions, on average, move to a defined lattice site, and the crystal lattice is fixed after the implantation damaging.

Most synthesis processes, including annealing above 800 °C [59], result in an amorphous or graphitic layer on the diamond surface. The latter is detrimental to fluorescence because it is opaque to emission wavelengths and it causes fluorescence quenching, namely an increase in the non radiative decay rate. A number of studies point out that the surface defects are likely to act as electron traps, so that both the charge stability and the emission properties of the NV center are negatively affected [65, 66]; this holds true in particular for small nanocrystals, where the surface plays a major role.

An effective solution to the presence of sp_2 carbon consists of air oxidation at about 600 °C-700 °C [65, 66], which simultaneously promotes oxygen surface termination, with positive consequencies for the negative charge stabilization of NV centers. Alternative approaches are acid cleaning or plasma treatment.

2.5 Applications

The NV^- center can be employed in a range of technological and scientific applications; the main focus of the present work is the single photon emission, which enables quantum cryptography implementation at room temperature [11]. The radiative decay $^3E \rightarrow {}^3A_2$ with non resonant pulsed pumping is exploited. Repetition rates from a single center are limited to few MHz by the long lifetime, with the possibility of cavity-based lifetime reduction. Collection lenses or grating are routinely employed to enhance the effective brightness.

Perhaps the most attractive room temperature characteristic of NV^- centers is the long spin coherence time, which allows to think of quantum information processing and storage applications. Indeed, photon information can be coherently transferred to the spin state of the center, and more importantly to the neighbouring and individually addressed ^{13}C or ^{14}N nuclear spins [10, 67]. As a result, a quantum register can be built. Two-qbit gates using the NV^- spin and neighbouring nuclear spin for quantum computation can be realized [68–70]. Furthermore, NV^- spin readout techniques have evolved to advanced single-shot processes [71], allowing fast information retrieval.

Photonic quantum simulation is another path towards information processing. However, one of the main problems when using NV centers as single photon sources in this context is that the ZPL accounts for $\sim 3\%$ of the total emission, whereas indistinguishable photons (with equal spectum) are required. This is why a cavity is often used to enhance the fraction of photons from the ZPL; on the contrary, the cavity is not necessary for microwave spin state manipulation.

Besides quantum information, NV centers are appealing for sensing purposes: the branch splitting of the spin sublevels is exploited for magnetic sensing in biological samples [72], electric field sensing [73], and temperature sensing [74]. The sensitivity to the magnetic field, for example, can be leveraged for drift measurements in a microfluidic channel [75], and, of course, spin sensing. For all sensing applications it is crucial that the centers lie within 10 nm from the surface, as their depth affects both the sensitivity and the spatial resolution. 5 nm nanodiamonds are often used for this reason.

Chapter 3

Materials and methods

3.1 HBT setup

Setup description The optical setup employed in the present work consists of an HBT time coincidence unit integrated in a confocal fluorescence microscope. A scheme is reported in figure 3.1. The excitation beam, in the region $510\,\mathrm{nm} < \lambda < 543\,\mathrm{nm}$, is spectrally filtered to remove long wavelength tails, and focused onto the sample through a high numerical aperture ($NA = 0.95$) microscope objective. The fluorescence with $\lambda > 550\,\mathrm{nm}$ originating from the sample is then collected through the same objective, and transmitted by the dichroic mirror. Further spectral filtering (typically with transmission at $\lambda > 600\,\mathrm{nm}$) is necessary to completely eliminate the residual laser light. Moreover, fluorescence photons are focused onto a $50\,\mathrm{\mu m}$ pinhole aperture that acts as a spatial filter. Since the pinhole aperture is the conjugated point of the excitation spot on the sample, any unwanted fluorescence from out of focus sources is blocked. IR filters after the beam splitter BS2 have a cutoff wavelength at $\lambda = 750\,\mathrm{nm}$, and can be found in an equivalent setup in the literature [76]. The obvious purpose is to narrow the collection spectral band down to the desired signal window, so that the background from the setup is maximally limited. A less obvious reason, which will be discussed below, is that they are effective in eliminating the optical crosstalk between the two single photon detectors. Finally the spatially and spectrally filtered signal is focused onto the active surface of two Single Photon Avalance Diodes (SPAD) after the beam splitter, as required by the HBT protocol. Time coincidences between single photon events are then recorded.

The strength of a confocal configuration is the spatial selectivity of the signal. On one hand, this is achieved by focusing the excitation beam to a diffraction-limited area. In this work, the excitation beam waist on the sample is $w_{exc} \approx 0.9\,\mathrm{\mu m}$ (see figure 3.2). As far as spatial accuracy is concerned, the sample drift and the translational stages with micrometric resolution are the currently limiting factors of our setup. On the other hand, the spatial filter in the collection line further limits

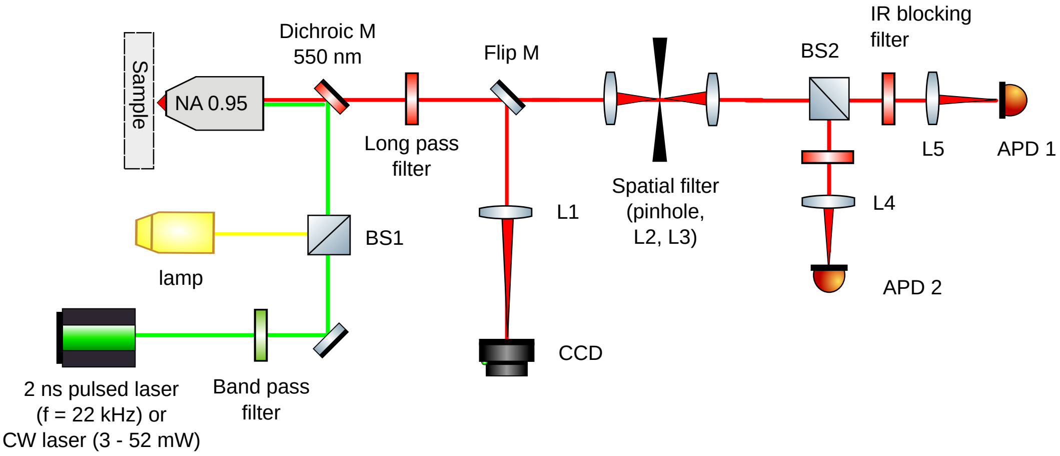

Figure 3.1: Scheme of the setup employed in the present work. BS: beam splitter, L: lens, NA: numerical aperture, M: mirror, CCD: charge-coupled device, APD: avalanche photo-diode.

background noise, that is exceptionally harmful to low intensity measurements.

An imaging system based on an incoherent source (lamp) and a CCD is added to the same setup. Its main aim is to provide a tool for the correct sample positioning along the focus axis ($\hat{z}$); furthermore, if super-micrometric clusters or dust grains are present, they can be easily seen and avoided. When the sample is conjugated to the CCD, or equivalently, its image is correctly focused, then the pinhole and the detectors are conjugated to one point of the sample.

A pulsed laser is exploited to perform time-resolved photoluminescence measurements for lifetime detection, whereas Continuous Wave (CW) excitation is the choice for coincidence measurements (HBT). Pulsed coincidence measurements are widely employed in the literature, but require repetition rates beyond MHz, which are orders of magnitude higher than the available one (22 kHz).

Specifications For pulsed excitation, a SuperK Compact supercontinuum laser by NKTphotonics is employed. The pulse duration is around 2 ns, with variable repetition rate up to 22 kHz. Time jitter between subsequent pulses is in the order of 1 µs. The emission ranges from 450 nm to 2400 nm. For the purposes of the experiment, only a 10 nm-FWHM band peaked $\lambda = 510$ nm is selected by a spectral filter (Thorlabs FB510-10). The resulting average power, after filtering, at maximum repetition rate, is $P \approx 180\,\mu\text{W}$.

As for CW excitation, a He-Ne green laser ($\lambda = 543$ nm) with nominal power $P = 4$ mW is initially used. 1 mW should be enough to perform the experiment, according to previous reports in the literature [47]. However, a second source is

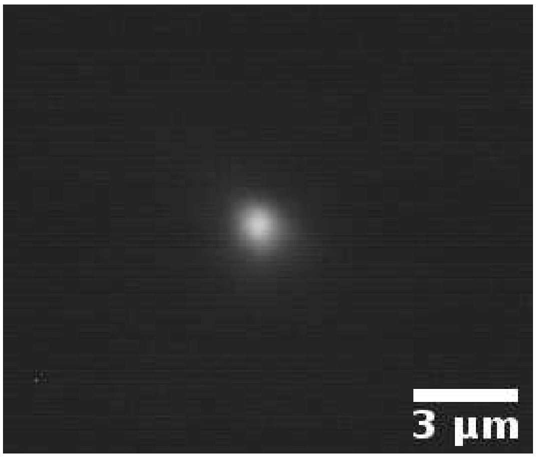

Figure 3.2: Fluorescence CCD image from a high concentration ND sample. The width of the excitation spot (beam waist) is $w_{exc} \approx 0.9\,\mu\mathrm{m}$. The diode laser at $\lambda = 520\,\mathrm{nm}$ is used for the excitation.

used to reach 50 mW excitation. The latter is a diode laser emitting at $\lambda = 520\,\mathrm{nm}$ (MatchBox 520L-13A). In both cases, further spectral filtering is necessary to remove long frequency components from the laser beam (Newport HPX535-40).

The spatial filter is made of a 5x/0.09 focusing objective, followed by a 50 µm diameter pinhole on a three axis micrometric translational stage and a 40 mm focal length lens. Assuming an incoming beam waist in the order of $w_{in} \sim 1\,\mathrm{mm}$ and an objective focal length $f \sim 40\,\mathrm{mm}$, the optimal pinhole diameter would be approximately $d \sim \lambda f / w_{in} \approx 27\,\mu\mathrm{m}$. As a first step a larger pinhole is chosen in order to be sure not to block part of the signal.

The two detectors are silicon Single Photon Avalanche Diodes (COUNT-T 100 by Laser Components). Their main figures of merit are: efficiency ($\eta_{det} \approx 60 \div 70\%$ at $600\,\mathrm{nm} < \lambda < 800\,\mathrm{nm}$), dark count rate (nominally $R_{dark} < 100\,\mathrm{cps}$, but actual dark counts are three times lower), time resolution ($\Delta t_{det} \approx 350\,\mathrm{ps}$), dead time ($t_{dead} \approx 42\,\mathrm{ns}$), and afterpulsing probability (1%). Because of the Si bandgap, the detectors are insensitive to photons at wavelengths $\lambda > 1.1\,\mu\mathrm{m}$. The active surface is approximately 100 µm wide, so that the collected fluorescence must be focused on it. This is achieved with the two 50 mm focal length lenses.

The correlation unit is an 8 channel time-to-digital converter (qTau, by qTools). Its temporal bin width is $\Delta t_{corr} = 162\,\mathrm{ps}$. The possible processing modes are: (i) start-stop, (ii) start-multistop, and (iii) cross correlation computations, whose differences are shown in figure 3.3. In lifetime measurements, each laser pulse triggers a start-multistop acquisition, whereas in HBT measurements cross-correlation between the events from the two detectors is recorded.

The imaging setup is calibrated using a reference patterned sample for atomic force microscopy. The true dimensions of such patterns are obtained through Scan-

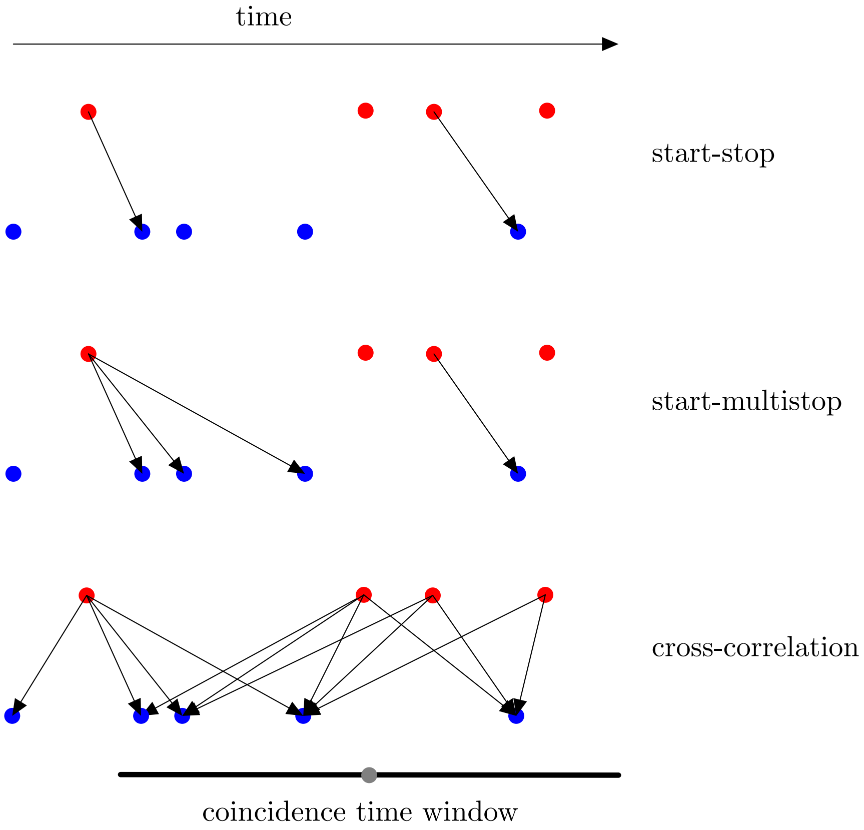
time
start-stop
start-multistop
cross-correlation
coincidence time window

Figure 3.3: Scheme of the three different coincidence processing modes. Start events are represented by red points, stop events by blue points. Each arrow corresponds to a coincidence event that populates the histogram.

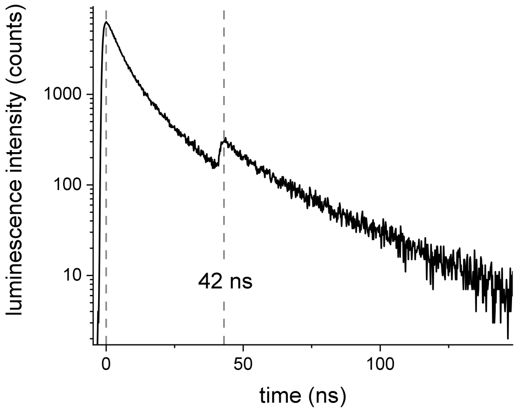

Figure 3.4: Effect of the 42 ns dead time on lifetime measurements with a slightly too high count rate: a second peak can be clearly seen, when the detectors, on average, start working again after being blinded by the first photons of the pulse.

ning Electron Microscopy (SEM). With the Leitz 100x/0.95 objective, and a 350 mm focal length lens in front of the CCD, the image calibration yields 54.5±0.4 nm/pixel.

Measurement protocol: lifetime Lifetime measurements are employed to identify the fluorescence from NV centers. The time dependent intensity following a short pulsed excitation is fitted with an exponential decay, whose characteristic time τ is the lifetime of the NV excited state. As a result a histogram of start-multistop events is acquired, where the laser trigger signal acts as the start, and the detected photons in one (or even both) of the SPADs act as the stop events. Each column of the histogram represents the number of start-stop coincidences with a specific delay. Simple start-stop acquisition is not the most appropriate choice for the recording of a time dependent intensity because the first stop event hides all the following ones until a new start is received.

Since the detector dead time (42 ns) is non negligible with respect to the NV^- lifetime (~ 25 ns), precautions must be taken not to artificially modify the photon arrival statistics. Indeed, if the photon flux is large enough, the first photons of the laser pulse make the detector completely blind for the following 42 ns. Thus a peak around zero turns up, plus one or more additional peaks that point out the time at which, on average, the detector starts working again (see figure 3.4). A low photon flux should be exploited in order to avoid the abovementioned artefact; ideally, a negligible percentage of pulses should be seen containing more than one photon by the detectors. This is why in the present work the count rate is usually kept below 1 kHz when working in pulse mode with 22 kHz repetition rate. In such conditions, start-stop and start-multistop histograms are equivalent.

Measurement protocol: HBT Regarding HBT measurements, a cross correlation histogram is built. In practice, time differences between any start and any stop are computed within a specified time window. The histogram of such time differences, if normalized, represents the second order correlation function $g^{(2)}(\tau)$. Normalization consists in dividing by the number of random coincidences for uncorrelated events, that is $N = R_1\, R_2\, \Delta t_{bin}\, t_{meas}$, where R_1 and R_2 are the count rates of the two detectors, Δt_{bin} is the bin width, and t_{meas} the acquisition time of the measurement. In HBT histograms with CW excitation the effect of dead time is not relevant because there are not intensity peaks, but rather approximately constant photon fluxes, so that the problem arises only close to saturation (2×10^7 cps).

Measurement protocol: remarks Before a measurement session, a highly and homogeneously fluorescent sample is focused using CCD imaging. The fluorescence spot diameter is checked (see figure 3.2), and then the detector count rates are iteratively maximized as a function of pinhole and detector positions along the three axis. This procedure should guarantee the alignment, and therefore proper working of the confocal setup.

A thorough measurement with confocal setup requires a raster scanning stage, with submicrometer precision, on which the sample is mounted [33]. Alternatively, the raster scan can be performed by slightly deflecting the beam before the microscope objective with a mirror mounted on piezo actuators [76]. Such devices allow to obtain fluorescence intensity maps of the sample, in principle equivalent to a fluorescence CCD image, but making use of the sensitivity of single photon detectors, thus enabling the localization of single NV-centers. Furthermore, more complex data can be obtained with spatial resolution, such as lifetime maps [77], and, in principle, HBT maps. In the present setup the scanning stage is not mounted yet. Nonetheless, HBT antibunching can be observed all the same by moving a sample with few NV-centers until a spatial count rate peak can be seen, and recording coincidences from such fluorescent spot.

Unfortunately, with the present setup lifetime can be easily retrieved for single centers only with repetition rates in the order of MHz. Consequently, the identification procedure through lifetime measurement is limited to relatively concentrated samples. For a simultaneous HBT and lifetime measurement, antibunching should be observed at different laser powers; the width of the exponential dip ($1/a$ in equation 1.10) at vanishing pump power ($k_{21} \to 0$) corresponds to the lifetime of the first excited state (see equation 1.18).

SPAD: working principles Silicon diodes, polarized above breakdown voltage, can be used as single photon detectors: when a photon crosses the depletion region it can be absorbed with simultaneous generation of an electron-hole pair; the primary pair is accelerated by the strong electric field and in turn generates further pairs in an avalanche process. The resulting electric current is recorded as the signal of the incoming photon. After reaching a threshold current the avalanche is quenched, both passively – thanks to the intrinsic resistance of the device, which causes a voltage drop – and actively, that is, by adding a specific external circuit with the purpose of extinguishing the avalanche and subsequently restoring the working voltage. During the avalanche, and until initial voltage is restored, the detector is at least partially blind, that is, incoming photons can not trigger a new avalanche and generate a signal. The quenching circuit of commercial devices is usually designed so that the detector is either active, or totally blind. In this way, the exponential recovery of sensitivity after the avalanche quenching is avoided.

SPAD: noise sources A SPAD has two main noise sources. *Dark counts* represent the first one: charge carriers thermally generated in the depletion region trigger avalanches, resulting in randomly distributed counts, indistinguishable from external events. All other sources are said to be of correlated noise, that is, the "false" photon closely follows another event. *Afterpulsing* represents the most relevant source of correlated noise: trapped charge carriers from a previous avalanche can be released after non-negligible time, and initiate a second avalanche. This why a long dead time is often priviledged: since trapped carriers decay exponentially with time, the delay in restoring the working voltage prevents most of the afterpulsing events.

With SPAD arrays, an additional type of correlated noise is reported in the literature: *crosstalk* [78]. The effect arises whenever a SPAD pixel, during its avalanche, produces secondary photons that travel to the active area (or even the undepleted area) of the neighbouring pixel from where they trigger a spurious avalanche. If the detector is not an array, but rather a single diode, as in our case, the probability that secondary photons from the first detector enter the active area of the second one is far lower than in arrays, but not null. Indeed, several sudies report on the photoemission from breakdown operated diodes for photodetection [79–81]. In particular, Ingargiola et al. [80] leverage secondary photons luminescence to investigate the temporal propagation of a photon-triggered avalanche within the device.

Optical crosstalk By removing the IR blocking filters in our setup after the beam splitter (see figure 3.1) optical crosstalk turns up. The effect is seen in the HBT histogram as an excess of coincidence counts with specific delay (typically, between $\tau = \pm 7\,\mathrm{ns}$ and $\tau = \pm 12\,\mathrm{ns}$). The characteristic double peak can be seen in figure 3.6a. The effect can be explained by secondary photon generation in the first SPAD, around 6.5 ns after the arrival of the triggering photon. A portion of the emission is collimated by lens 4 and 5 (see figure 3.1), travels back to the last partially reflecting element (for example filters or the pinhole), and returns to the detectors, where it is focused again onto the active area. At that time only the second SPAD is active: dead time prevents the first SPAD from recording its own secondary photons. As a consequence crosstalk coincidences are seen in $g^{(2)}(\tau)$.

To support this claim, the shift of the double peak with respect to zero is plotted

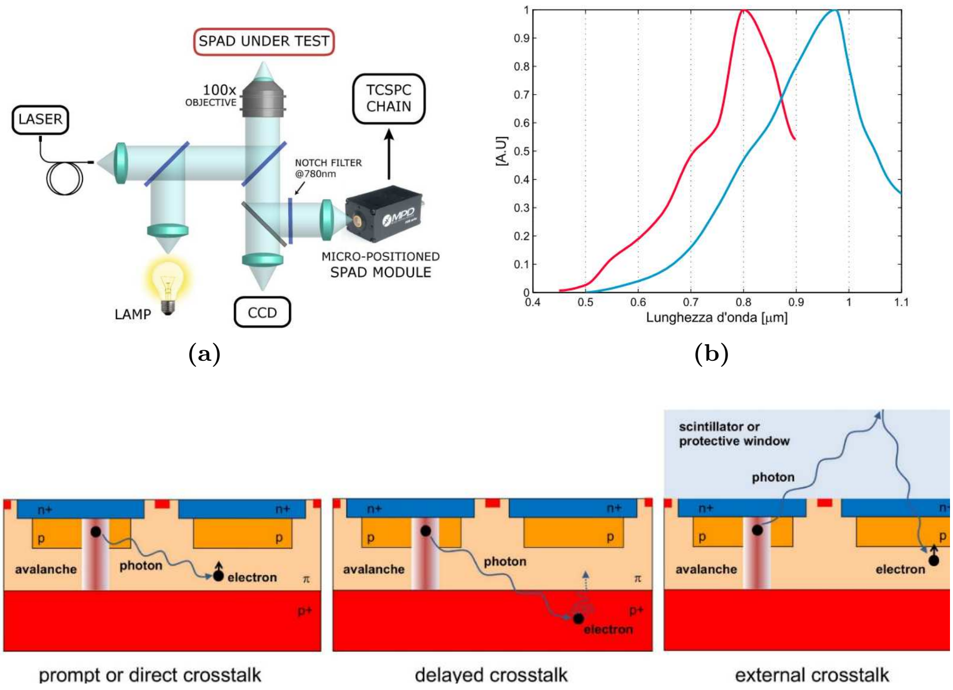
SPAD UNDER TEST
100x
OBJECTIVE
LASER
TCSPC
CHAIN
NOTCH FILTER
@780nm
MICRO-POSITIONED
SPAD MODULE
LAMP
CCD
MPD
[A.U]
1
0.9
0.8
0.7
0.6
0.5
0.4
0.3
0.2
0.1
0
0.4
0.5
0.6
0.7
0.8
0.9
1
1.1
Lunghezza d'onda [µm]
scintillator or
protective window
n+
p
avalanche
photon
electron
π
p+
prompt or direct crosstalk
delayed crosstalk
external crosstalk

(a)

(b)

(c)

Figure 3.5: (a) Confocal setup assembled by Ingargiola et al. [80] to study luminescence timing within a SPAD avalanche. (b) Two different measurements of the luminescence spectrum of an avalanche photodiode in breakdown [81]. The main emission peak can be seen in the NIR region. (c) Scheme of the possible crosstalk processes in a typical SPAD array [78].

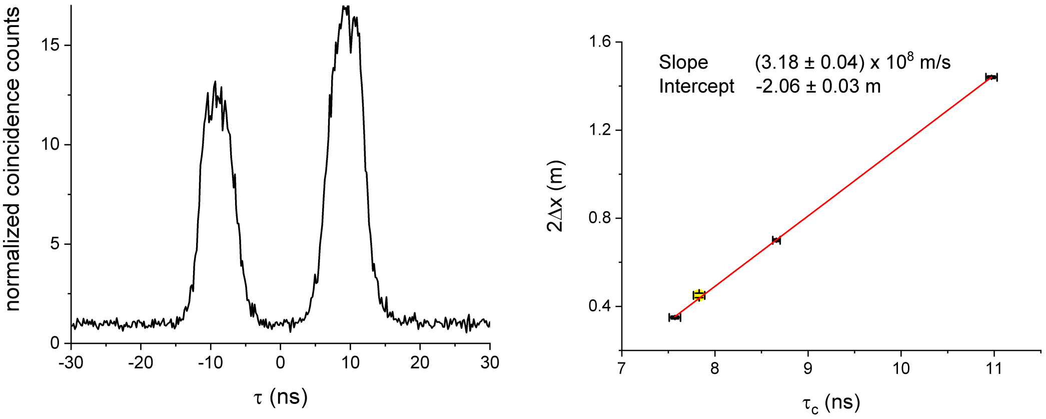

(a) **(b)**

Figure 3.6: (a) Typical HBT histogram with crosstalk peaks around $\tau = \pm 10\,\mathrm{ns}$. The more unbalanced the count rates between the two detectors, the more asymmetric the coincidence histogram. In this case, for example, if $\tau = t_B - t_A$, detector A has a slightly larger count rate; this is consistent with the secondary photon hypothesis: more crosstalk photons are produced in A and afterwards detected by B than viceversa. On the contrary, any external signal should generate a symmetric $g^{(2)}(\tau)$ because the beam splitter is symmetric itself (50:50, not frequency- nor polarization-selective). (b) Linear fit of twice the distance Δx between the detectors and the last partially reflecting element as a function of the peak centroid τ_c in the coincidence histogram. The last partially reflecting element is a neutral density filter but for the yellow-highlighted point, which represents a measurement with the spatial filter last (the distance pinhole-detector is considered).

together with twice the distance between the detector and the last partially reflecting element (either a neutral density filter or the pinhole) in figure 3.6b. The linear fit slope ($\sim c$) is a clear evidence of the presence of photons travelling back and forth between the two events of a crosstalk coincidence. The artefact can be seen with any continuous light source producing a reasonable number of counts in the detectors ($> 1\,\mathrm{kcps}$).

3.2 Nanodiamonds

Commercial fluorescent NanoDiamonds (ND) by Sigma Aldrich are used to test the setup. Average nominal size is 100 nm whereas NV density is 3ppm. NDs are originally dispersed in deionized water. For photoluminescence measurements they are diluted, disaggregated with ultrasounds, and drop-casted on a silicon substrate. No ligand is used to attach them to the surface.

Assuming the NV density specified by the manufacturer, a spherical ND containing on average 1 NV center should have a diameter of $\sim$ 15 nm. A 100 nm diameter sperical ND should contain ~ 275 centers, instead. As a consequence, the NDs potentially producing antibunched photons are found in the low size tail of the distribution: for $g^{(2)}(\tau) < 0.9$, NDs with approximately $d \leq 30\,\mathrm{nm}$ could be accepted, for example (no background noise is taken into account when estimating the amplitude of the antibunching dip, in this case).

In order to reduce the size dispersion some centrifugation attempts were made; however, we found that the more the NDs are centrifugated and sonicated, the dirtier is the deposited droplet as seen with a Scanning Electron Microscope (SEM). As the dirtiness of the sample increases, the identification of NDs becomes more and more difficult even in SEM images. During optical measurements a portion of this non-diamond matter fluorescences, and is usually identified because it photobleaches within seconds. In addition, it is difficult to precisely select NDs smaller than 30 nm but larger than 15 nm with a centrifugation process. Consequently, droplets of non-centrifugated NDs, containing NDs of different sizes, were priviledged.

In order to isolate single centers, commercial single digit NDs (with $N < 4$, for example) will be needed. In this preliminary work, larger NDs are chosen because the presence of a visible signal is required in the first stages of the experiment.

A few substrates have been considered for ND deposition. Silicon has the advantage of being conductive, so that SEM observation is easier. Moreover, microscope slides, coverslips and silica show much higher background count rates. This fact might be due to light scattering and fluorescence collection through total internal reflection along the whole substrate.

In order to isolate single NDs, the sonicated solution is drop-casted on a Si wafer, and afterwards covered with another Si wafer while drying. The result of this deposition process can be seen in figure 3.7b.

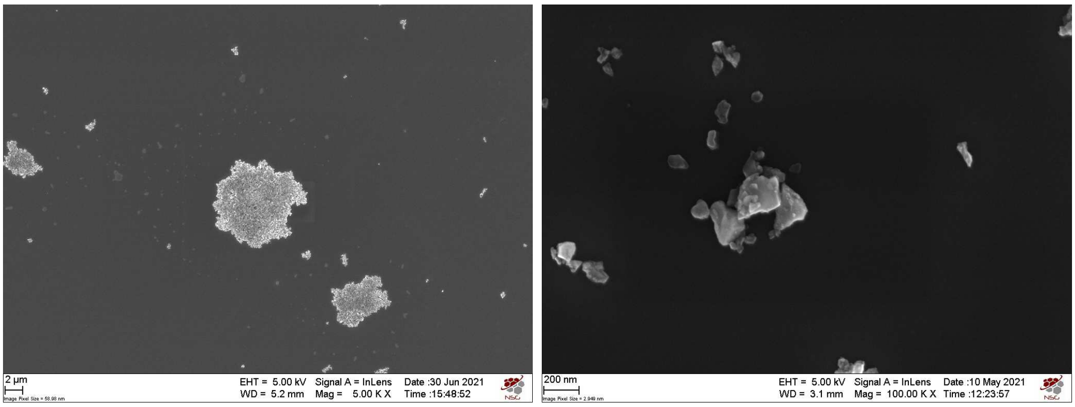
2 µm
Image Pixel Size = 58.98 nm
EHT = 5.00 kV
Signal A = InLens
Date :30 Jun 2021
WD = 5.2 mm
Mag = 5.00 K X
Time :15:48:52
NSG
200 nm
Image Pixel Size = 2.949 nm
EHT = 5.00 kV
Signal A = InLens
Date :10 May 2021
WD = 3.1 mm
Mag = 100.00 K X
Time :12:23:57
NSG

(a) **(b)**

Figure 3.7: Scanning Electron Microscope (SEM) images of NDs from Sigma Aldrich deposited on a Si substrate. In (a) a typical micrometric cluster of non-sonicated NDs can be seen, whereas in (b) single NDs can be distinguished (1 h ultrasound, dried between two Si wafers); small NDs still appear to be attached to larger ones, but on the whole, the deposition is successful. A remarkable size dispersion can be appreciated in (b).

Chapter 4

Results and discussion

Lifetime and spectrum A typical ND lifetime is shown in figure 4.1a. The double exponential fit is:

$$I(t) = A_1 e^{-\frac{t}{\tau_1}} + A_2 e^{-\frac{t}{\tau_2}} \tag{4.1}$$

The longer lifetime $\tau_2 \approx 25\,\mathrm{ns}$ is in agreement with the expected value for the zero-spin projection of the NV$^-$ triplet of excited states in NDs [41]. The short component $\tau_1 \approx 8.6\,\mathrm{ns}$ could be accounted for by the $m = \pm 1$ spin projections of the same triplet, although no quantitative agreement with the value reported by Neumann et al. ($\tau_1 \approx 12.7\,\mathrm{ns}$) [46] can be found. This hypothesis is supported by the comparable amplitude of the two components: $A_1/A_2 \approx 3$, whereas $A_1/A_2 = 2$ would be expected if the three spin projections had the same population after the pump pulse.

For all spin projections, the lifetime can be strongly affected by density of optical states in the surrounding environment, and by competing decay channels, such as those related to surface quenching and phonon mediated transitions. The consequence is usually a broadening of the lifetime distribution when considering different centers, as pointed out by several groups [42, 43, 77, 82].

There might be other defects, such as color centers with silicon, or surface defects [63], contributing to shorter lived fluorescence, as well.

It should be noticed that the $m = \pm 1$ spin projections might contribute to fluorescence in lifetime measurement (pulsed mode with $f = 22\,\mathrm{kHz}$) but not to CW $g^{(2)}(\tau)$ due to the optical spin polarization mechanism.

For completeness of characterization a luminescence spectrum is shown in figure 4.1b. This is acquired in CW excitation ($P = 52\,\mathrm{mW}$, $\lambda = 520\,\mathrm{nm}$) with a high concentration sample of NDs deposited on Si. Luminescence is collected at $\lambda > 550\,\mathrm{nm}$. The ZPLs of both NV^0 and NV$^-$ can be seen, as well as their phonon sideband, indicating that both charge states are present during an HBT measurement. The maximum emission occurs at $\lambda \approx 660\,\mathrm{nm}$, although it is not possible to distinguish the luminescence of the two charged states around 650 nm.

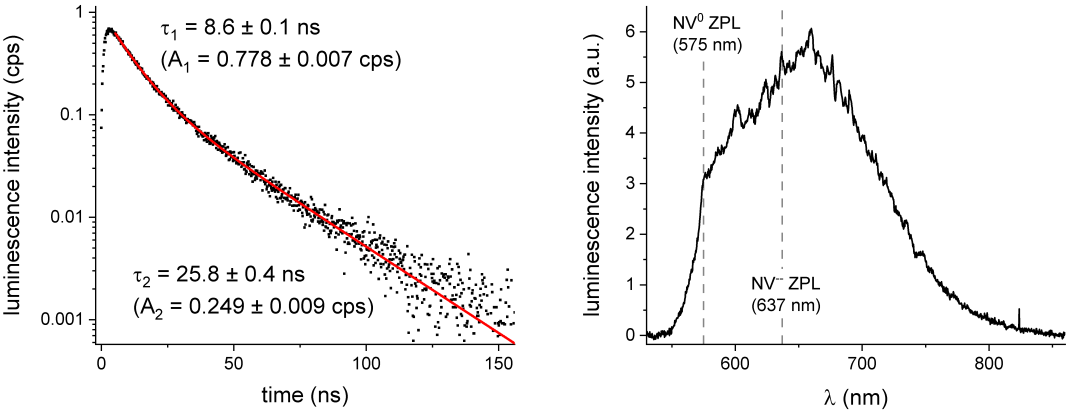

(a) **(b)**

Figure 4.1: (a) Typical lifetime from a ND cluster at $\lambda_{collect} = 700 \pm 5\,\text{nm}$. The fit is bi-exponential with decay times and amplitudes of the two components displayed in the figure. (b) Spectrum of a highly concentrated ND sample. The expected zero phonon lines of neutral and negativly charged NV centers are highlighted.

HBT Five instances of antibunching were obtained in four different spots of the samples, labelled α, β, γ, and δ. The experimental $g^{(2)}(\tau)$ relative to peak β is shown in figure 4.2. Due to the high noise compared to the antibunching signal, the fit is performed using the model for two-level systems, that is:

$$g^{(2)}(\tau) = 1 - Ae^{-a|\tau|} \quad A, a > 0 \tag{4.2}$$

In fact, although more appropriate for NV-centers, a three-level system model, such as that in equation 1.10, has too many parameters to fit.

Besides neglecting the bunching of a three-level system, the fitting function in equation 4.2 does not take into account the presence of a spin triplet, with different lifetimes among the sublevels. However, in CW excitation, optical spin polarization should occur, so that mainly the zero spin projection should be occupied.

In table 4.1 a summary of all antibunching instances is shown. The significance of the signal can be seen by considering $A = 0$ as the null hypothesis: if a rejection limit of 3σ is set, in 4 cases out of 5 the null hypothesis can be rejected, providing evidence of antibunching observation. Further support comes from the dip width (or characteristic time) $1/a$, that is consistently found around 6 ns. As expected, the latter is smaller than the lifetimes of NV-center first excited levels $1/a < \tau_2$ (see equation 1.17), both with $\tau_2 \approx 25\,\text{ns}$ and $\tau_2 \approx 12\,\text{ns}$. The result is also consistent with what is found by Beveratos et al. [47], that is $1/a \approx 8\,\text{ns}$ at $P \gtrsim 1\,\text{mW}$, decreasing with pump power. However, the data are too noisy to enable lifetime estimation: although the β spot antibunching looks narrower at higher pump power,

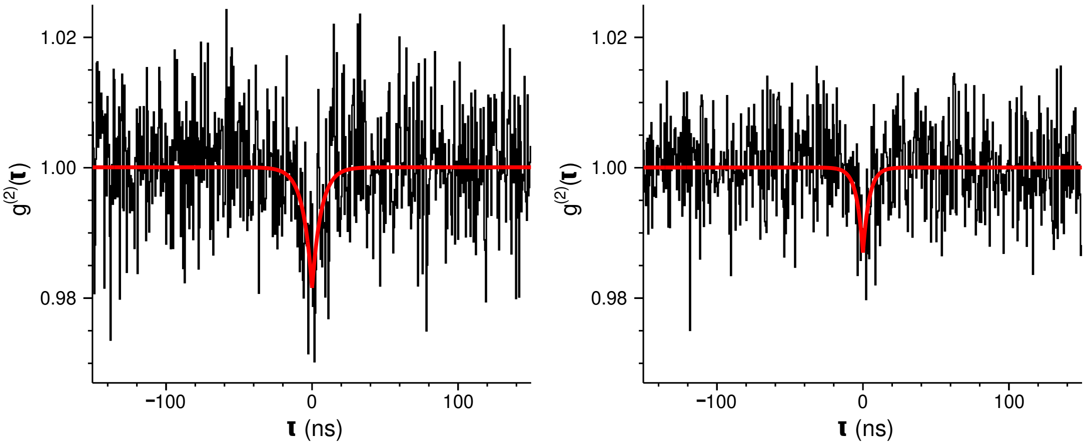

(a) **(b)**

Figure 4.2: Two examples of the most promising coincidence measurements. The two histograms refer to peak β (sample 1), excited with a nominal power of 20 mW (a) and 52 mW (b) (recall that the effective power is slightly less than $P/2$ due to the loss at the beam splitter BS1). The bin width in this picture is 486 ps. No offset time parameter is added to the fit because detector positioning is precise enough: 1 cm displacement of one SPAD would result in a 33 ps translation of $g^{(2)}(\tau)$.

spot	λ_{coll} (nm)	P (mW)	R (kcps)	t_{int} (s)	A	$1/a$ (ns)
α (1)	[655, 720]	20	[40, 60]	160	0.07 ± 0.02	8 ± 3
β (1)	[655, 720]	20	[70, 130]	2630	0.019 ± 0.003	6 ± 1
β (1)	[655, 720]	52	[140, 210]	1870	0.013 ± 0.003	4 ± 1
γ (2)	[610, 750]	30	[150, 180]	4000	0.007 ± 0.002	7 ± 2
δ (1)	[610, 750]	10	[60, 150]	1660	0.010 ± 0.005	5 ± 4

Table 4.1: Measurements of the antibunching dip of the fluorescent spots labelled as α, β, γ and δ on samples 1 and 2. A is the amplitude of the antibunching dip, whereas $1/a$ is an estimate of its width. Only δ is compatible with the null hypothesis $A = 0$ once the 3σ critical value is established for rejection. The reported experimental parameters are: collection spectral band λ_{coll}, nominal power P emitted by the laser (before the beam splitter BS1), count rate R (an interval is pointed out due to fluctuations during the measurement), and integration time t_{int}. A SEM image of sample 1, in a region with relatively higher ND concentration than in measured spots, can be seen in figure 3.7b.

no statistically meaningful statement can be made regarding its width. Likewise, extracting the dip width at vanishing pump power is still not feasible.

The integration time, which could be helpful in reducing the noise, is currently limited by the mechanical drifts between the sample and the objective lens. The drift results in count rates with considerable oscillations, typically within 10 min time (see table 4.1). If the luminescence spot is lost due to drifts, it is usually not possible to recover the same measurement conditions, so that mainly short runs are saved.

The other major path to enhance the signal quality is to reduce the background and increase the absolute counts from NDs. At the moment the background is perfectly proportional to nominal laser power; it accounts for 1 kcps per mW of nominal power when collection occurs in $655\,\text{nm} < \lambda_{collect} < 720\,\text{nm}$, and 5 kcps per mW of nominal power[1] for $610\,\text{nm} < \lambda_{collect} < 750\,\text{nm}$. A study of the dependence of the Signal to Noise Ratio (SNR) on the spectral band is therefore needed. Likewise SNR should be maximized as a function of pump power, too. To this regard Beveratos et al. [47] report that an optimal SNR (with single NV-center signal in ND around 20 kcps and background $\sim$ 2 kcps) is found around 2 mW pump power, that is approximately the NV-center saturation power. Of course direct comparison of pump powers does not take into account possible differences in the focalization of the beam, and so in the effective excitation intensity. Finally, as mentioned in section 3.1, the spatial filter selectivity can be improved, potentially leading to a significant increase in the SNR.

From the antibunching amplitude it is possible to estimate the number of probed color centers: N perfect emitters in an ideal setup would result in $A = 1/N$. On the other hand, additional classical background significantly reduces antibunching: consider N emitters in a setup with a background count rate equivalent to further M emitters. Two cases can be identified:

- a “signal” photon (that is, generated by one of the N emitters) triggers an event in detector 1. This occurs with probability $N/(N+M)$ among the events in detector 1. Then, the probability of recording a zero delay coincidence, that is, a simultaneous photon in detector 2, conditioned to the signal photon recording in 1, is reduced by $1/(N+M)$ with respect to independent events (infinite delay coincidence). In other words, available emitters for photon 2 are $N-1$ plus the background;

- a background photon triggers an event in detector 1. This occurs with probability $M/(M+N)$. Then the recording of a simultaneous event in detector 2 is independent of the triggering of detector 1. As a result the probability of a zero delay event in 2, conditioned to the detection in 1, is the same as for infinite delay.

---

[1] Consider also that the filters employed for the [610 nm, 750 nm] band have a better transmission.

spot (sample)	P (mW)	$\max[R_s + R_b]$ (kcps)	R_b (kcps)	N	R_s/N (kcps)
α (1)	20	60	20	6	6.7
β (1)	20	130	20	39	2.8
β (1)	52	210	50	44	3.6
γ (2)	30	180	150	4	7.5
δ (1)	10	150	50	46	2.2

Table 4.2: Rough estimate of the number of NV-centers N in the luminescent spots α to δ. The maximum total count rate during the run $\max[R_s + R_b]$ is reported, along with the approximate background count rate R_b. Finally, an order of magnitude for the signal count rate per center is obtained. The reference value for the latter is ~ 20 kcps in nanodiamonds and ~ 50 kcps in bulk diamond films, whereas background is around 1 kcps in the most favourable conditions, as reported by Beveratos et al. [47]. As a result, if our estimates are reliable enough, some improvement is necessary in terms of both signal enhancement and background reduction.

This means that the depth of antibunching must be $A = N/(N+M)^2$. Equivalently, given A, one can estimate the number of single emitters:

$$N = \left(\frac{N}{N+M}\right)^2 \frac{1}{A} \tag{4.3}$$

where $N/(N+M)$ is the ratio of signal counts to total counts. In table 4.2 the estimated number of centers in luminescent spots α to δ is reported. The computation reliability is limited by several factors, among which the errors in the spot positioning, the drifts with the related variable signal count rate, and the assumption of classical background. Moreover, all NV centers are assumed to be equally bright, which might not be the case due to surface closeness and center orientation. As a result only orders of magnitude can be considered meaningful. Nonetheless, it is encouraging to notice that the two estimates of N for ND β are similar.

As described in section 3.2, the size of a spherical nanodiamond can be retrieved from N, assuming that all centers lie in a single nanodiamond. In our case, the two extremes, that is, $N \approx 4$ and $N \approx 40$, correspond respectively to $d \sim 25$ nm and $d \sim 50$ nm.

It is worth mentioning that Flagg et al. [83], when measuring $g^{(2)}(\tau)$, take into account the Instrumental Response Function (IRF), that is, the time response of the setup to a 5 ps Ti:sapphire laser. With such correction they obtain $g^{(2)}(0) \approx 0$ from an initial $g^{(2)}(0) \approx 0.5$. This is because the IRF is convoluted with the true correlation function in a measurement, thus flattening it out. However, the temporal averaging over the precision interval is relevant in their experiment since the investigated features are about 250 ps wide. On the contrary, our temporal precision ($\Delta t_{det} \approx 350$ ps) is much higher than required to resolve a 6 ns wide antibunching dip. As a result, our $g^{(2)}(\tau)$ would not benefit from deconvolution of IRF.

Conclusions

The aim of the presented work was to observe the transition from classical to quantum regime in the emission from Nitrogen-Vacancy (NV) centers in nanodiamonds. The task was accomplished through photon time coincidence measurements, and is preliminary to the development of a solid state, room temperature single photon emitter.

In this work, the confocal fluorescence microscope with a HBT time coincidence module was successfully designed and tested. Lifetimes compatible with the expectation were obtained from commercial fluorescent nanodiamonds, thus confirming the dominance of the fluorescence originating from NV centers.

By characterizing the luminescence from NV centers in nanodiamonds, a first evidence of the onset of quantum regime, consisting of a small antibunching dip in the second order correlation function $g^{(2)}(\tau)$, was obtained. This result allowed us to extract an order of magnitude for the number of centers observed and for the single center luminescence intensity. Such preliminary results draw attention to the improvements in terms of both signal enhancement and background suppression, that are necessary for an optimal operation of the setup.

After optimization of the antibunching measurements the focus will be moved to the synthesis of the samples and their characterization as far as emission properties are concerned. Cavity coupling of the NV center in resonance with the main ZPL is desirable, since it boosts the generation of photons potentially useful for quantum information. The underlying principle in the development of a single photon source should be the simplicity of fabrication and of operation, which excludes cryogenic cooling, for example. Indeed, a scalable device is strongly requested by current and future scientific and technological applications.

Bibliography

[1]S. J. Freedman and J. F. Clauser, “Experimental Test of Local Hidden-Variable Theories”, Physical Review Letters **28**, 938–941 (1972).

[2]D. Bouwmeester, J.-W. Pan, K. Mattle, et al., “Experimental quantum teleportation”, Philosophical Transactions of the Royal Society of London. Series A: Mathematical, Physical and Engineering Sciences **356**, edited by A. Ekert, R. Jozsa, and R. Penrose, 1733–1737 (1998).

[3]A. Aspuru-Guzik and P. Walther, “Photonic quantum simulators”, Nature Physics **8**, 285–291 (2012).

[4]T. D. Ladd, F. Jelezko, R. Laflamme, et al., “Quantum computers”, Nature **464**, 45–53 (2010).

[5]N. Gisin, G. Ribordy, W. Tittel, and H. Zbinden, “Quantum cryptography”, Reviews of Modern Physics **74**, 145–195 (2002).

[6]J. Wang, F. Sciarrino, A. Laing, and M. G. Thompson, “Integrated photonic quantum technologies”, Nature Photonics **14**, 273–284 (2020).

[7]C. H. Bennett and G. Brassard, “Quantum cryptography: Public key distribution and coin tossing”, Theoretical Computer Science **560**, 7–11 (2014).

[8]H. Wang, J. Qin, X. Ding, et al., “Boson Sampling with 20 Input Photons and a 60-Mode Interferometer in a 1014 -Dimensional Hilbert Space”, Physical Review Letters **123**, 250503 (2019).

[9]E. Togan, Y. Chu, A. S. Trifonov, et al., “Quantum entanglement between an optical photon and a solid-state spin qubit”, Nature **466**, 730–734 (2010).

[10]S. Yang, Y. Wang, D. D. Rao, et al., “High-fidelity transfer and storage of photon states in a single nuclear spin”, Nature Photonics **10**, 507–511 (2016).

[11]A. Beveratos, R. Brouri, T. Gacoin, et al., “Single Photon Quantum Cryptography”, Physical Review Letters **89**, 187901 (2002).

[12]F. Bouchard, A. Sit, Y. Zhang, et al., “Two-photon interference: the Hong-Ou-Mandel effect”, Reports on Progress in Physics **84**, 012402 (2021).

[13]C. K. Hong, Z. Y. Ou, and L. Mandel, “Measurement of subpicosecond time intervals between two photons by interference”, Physical Review Letters **59**, 2044–2046 (1987).

[14]N. Somaschi, V. Giesz, L. De Santis, et al., "Near-optimal single-photon sources in the solid state", Nature Photonics **10**, 340–345 (2016).

[15]K. E. Dorfman, S. Asban, B. Gu, and S. Mukamel, "Hong-Ou-Mandel interferometry and spectroscopy using entangled photons", Communications Physics **4**, 1–7 (2021).

[16]J. W. Goodman, *Statistical Optics*, Wiley Series in Pure and Applied Optics (Wiley, 2015), p. 544.

[17]R. H. Brown and R. Q. Twiss, "Correlation between Photons in two Coherent Beams of Light", Nature **177**, 27–29 (1956).

[18]F. Boitier, A. Godard, E. Rosencher, and C. Fabre, "Measuring photon bunching at ultrashort timescale by two-photon absorption in semiconductors", Nature Physics **5**, 267–270 (2009).

[19]D. B. Scarl, "Measurement of Photon Time-of-Arrival Distribution in Partially Coherent Light", Physical Review Letters **17**, 663–666 (1966).

[20]A. Beveratos, R. Brouri, J.-P. Poizat, and P. Grangier, "Bunching and Antibunching from Single NV Color Centers in Diamond", Quantum Communication, Computing, and Measurement 3, 261–267 (2006).

[21]F. Kaneda, K. Garay-Palmett, A. B. U'Ren, and P. G. Kwiat, "Heralded single-photon source utilizing highly nondegenerate, spectrally factorable spontaneous parametric downconversion", Optics Express **24**, 10733 (2016).

[22]G. J. Mendoza, R. Santagati, J. Munns, et al., "Active temporal and spatial multiplexing of photons", Optica **3**, 127 (2016).

[23]M. D. Eisaman, J. Fan, A. Migdall, and S. V. Polyakov, "Invited Review Article: Single-photon sources and detectors", Review of Scientific Instruments **82**, 071101 (2011).

[24]H. Wang, Y. M. He, T. H. Chung, et al., "Towards optimal single-photon sources from polarized microcavities", Nature Photonics **13**, 770–775 (2019).

[25]D. Najer, I. Söllner, P. Sekatski, et al., "A gated quantum dot strongly coupled to an optical microcavity", Nature **575**, 622–627 (2019).

[26]N. Tomm, A. Javadi, N. O. Antoniadis, et al., "A bright and fast source of coherent single photons", Nature Nanotechnology **16**, 399–403 (2021).

[27]Z. X. Koong, E. Scerri, M. Rambach, et al., "Coherent Dynamics in Quantum Emitters under Dichromatic Excitation", Physical Review Letters **126**, 047403 (2021).

[28]S. Zhao, J. Lavie, L. Rondin, et al., "Single photon emission from graphene quantum dots at room temperature", Nature Communications **9**, 3470 (2018).

[29]T. Ihara, S. Miki, T. Yamada, et al., "Superior properties in room-temperature colloidal-dot quantum emitters revealed by ultralow-dark-count detections of temporally-purified single photons", Scientific Reports **9**, 15941 (2019).

[30]H. Utzat, W. Sun, A. E. K. Kaplan, et al., “Coherent single-photon emission from colloidal lead halide perovskite quantum dots”, Science **363**, 1068–1072 (2019).

[31]S. Morozov, E. L. Pensa, A. H. Khan, et al., “Electrical control of single-photon emission in highly charged individual colloidal quantum dots”, Science Advances **6**, eabb1821 (2020).

[32]A. Saxena, Y. Chen, A. Ryou, et al., “Improving Indistinguishability of Single Photons from Colloidal Quantum Dots Using Nanocavities”, ACS Photonics **6**, 3166–3173 (2019).

[33]H. Kaupp, C. Deutsch, H.-C. Chang, et al., “Scaling laws of the cavity enhancement for nitrogen-vacancy centers in diamond”, Physical Review A **88**, 053812 (2013).

[34]M. Ruf, M. Weaver, S. van Dam, and R. Hanson, “Resonant Excitation and Purcell Enhancement of Coherent Nitrogen-Vacancy Centers Coupled to a Fabry-Perot Microcavity”, Physical Review Applied **15**, 024049 (2021).

[35]G. Alagappan, L. A. Krivitsky, and C. E. Png, “Diamond in a Nanopocket: A New Route to a Strong Purcell Effect”, ACS Omega **3**, 4733–4742 (2018).

[36]S. Hu, M. Khater, R. Salas-Montiel, et al., “Experimental realization of deep-subwavelength confinement in dielectric optical resonators”, Science Advances **4**, eaat2355 (2018).

[37]J. A. Smith, C. Clear, K. C. Balram, et al., “Nitrogen-Vacancy Center Coupled to an Ultrasmall-Mode-Volume Cavity: A High-Efficiency Source of Indistinguishable Photons at 200 K”, Physical Review Applied **15**, 034029 (2021).

[38]A. Faraon, P. E. Barclay, C. Santori, et al., “Resonant enhancement of the zero-phonon emission from a colour centre in a diamond cavity”, Nature Photonics **5**, 301–305 (2011).

[39]K. Liu, S. Zhang, V. Ralchenko, et al., “Tailoring of Typical Color Centers in Diamond for Photonics”, Advanced Materials **33**, 2000891 (2021).

[40]J. T. Choy, I. Bulu, B. J. M. Hausmann, et al., “Spontaneous emission and collection efficiency enhancement of single emitters in diamond via plasmonic cavities and gratings”, Applied Physics Letters **103**, 161101 (2013).

[41]M. W. Doherty, N. B. Manson, P. Delaney, et al., “The nitrogen-vacancy colour centre in diamond”, Physics Reports **528**, 1–45 (2013).

[42]F. A. Inam, M. D. W. Grogan, M. Rollings, et al., “NV center emission in a substrate free low index environment”, Advances in Photonics of Quantum Computing, Memory, and Communication VI **8635**, 86350F (2013).

[43]J. Storteboom, P. Dolan, S. Castelletto, et al., “Lifetime investigation of single nitrogen vacancy centres in nanodiamonds”, Optics Express **23**, 11327 (2015).

[44]A. Batalov, C. Zierl, T. Gaebel, et al., “Temporal Coherence of Photons Emitted by Single Nitrogen-Vacancy Defect Centers in Diamond Using Optical Rabi-Oscillations”, Physical Review Letters **100**, 077401 (2008).

[45]L. Robledo, H. Bernien, T. V. D. Sar, and R. Hanson, “Spin dynamics in the optical cycle of single nitrogen-vacancy centres in diamond”, New Journal of Physics **13**, 025013 (2011).

[46]P. Neumann, R. Kolesov, V. Jacques, et al., “Excited-state spectroscopy of single NV defects in diamond using optically detected magnetic resonance”, New Journal of Physics **11**, 013017 (2009).

[47]A. Beveratos, R. Brouri, T. Gacoin, et al., “Nonclassical radiation from diamond nanocrystals”, Physical Review A - Atomic, Molecular, and Optical Physics **64**, 4 (2001).

[48]V. M. Acosta, A. Jarmola, E. Bauch, and D. Budker, “Optical properties of the nitrogen-vacancy singlet levels in diamond”, Physical Review B **82**, 201202 (2010).

[49]T. Plakhotnik, M. W. Doherty, and N. B. Manson, “Electron-phonon processes of the nitrogen-vacancy center in diamond”, Physical Review B - Condensed Matter and Materials Physics **92**, 1–5 (2015).

[50]M. Steiner, P. Neumann, J. Beck, et al., “Universal enhancement of the optical readout fidelity of single electron spins at nitrogen-vacancy centers in diamond”, Physical Review B **81**, 035205 (2010).

[51]A. Nizovtsev, S. Kilin, C. Tietz, et al., “Modeling fluorescence of single nitrogen–vacancy defect centers in diamond”, Physica B: Condensed Matter **308-310**, 608–611 (2001).

[52]L. Razinkovas, M. W. Doherty, N. B. Manson, et al., “Vibrational and vibronic structure of isolated point defects: The nitrogen-vacancy center in diamond”, Physical Review B **104**, 045303 (2021).

[53]Á. Gali, “Ab initio theory of the nitrogen-vacancy center in diamond”, Nanophotonics **8**, 1907–1943 (2019).

[54]R. Ulbricht, S. Dong, A. Gali, et al., “Vibrational relaxation dynamics of the nitrogen-vacancy center in diamond”, Physical Review B **97**, 1–6 (2018).

[55]S. Baier, C. E. Bradley, T. Middelburg, et al., “Orbital and Spin Dynamics of Single Neutrally-Charged Nitrogen-Vacancy Centers in Diamond”, Physical Review Letters **125**, 193601 (2020).

[56]N. Aslam, G. Waldherr, P. Neumann, et al., “Photo-induced ionization dynamics of the nitrogen vacancy defect in diamond investigated by single-shot charge state detection”, New Journal of Physics **15**, 013064 (2013).

[57]P. Siyushev, H. Pinto, M. Vörös, et al., “Optically Controlled Switching of the Charge State of a Single Nitrogen-Vacancy Center in Diamond at Cryogenic Temperatures”, Physical Review Letters **110**, 167402 (2013).

[58]S. Dhomkar, H. Jayakumar, P. R. Zangara, and C. A. Meriles, “Charge Dynamics in near-Surface, Variable-Density Ensembles of Nitrogen-Vacancy Centers in Diamond”, Nano Letters **18**, 4046–4052 (2018).

[59] E. A. Ekimov and M. V. Kondrin, "Vacancy–impurity centers in diamond: prospects for synthesis and applications", Physics-Uspekhi **60**, 539–558 (2017).

[60] D. Rani, O. R. Opaluch, and E. Neu, "Recent advances in single crystal diamond device fabrication for photonics, sensing and nanomechanics", Micromachines **12**, 1–22 (2021).

[61] J. Achard, V. Jacques, and A. Tallaire, "Chemical vapour deposition diamond single crystals with nitrogen-vacancy centres: a review of material synthesis and technology for quantum sensing applications", Journal of Physics D: Applied Physics **53**, 313001 (2020).

[62] L. Basso, N. Bazzanella, M. Cazzanelli, and A. Miotello, "On the route towards a facile fluorescent nanodiamonds laser-synthesis", Carbon **153**, 148–155 (2019).

[63] B. R. Smith, D. Gruber, and T. Plakhotnik, "The effects of surface oxidation on luminescence of nano diamonds", Diamond and Related Materials **19**, 314–318 (2010).

[64] H. B. Dyer and L. D. Preez, "Irradiation Damage in Type I Diamond", The Journal of Chemical Physics **42**, 1898–1906 (1965).

[65] R. Kumar, D. K. Singh, P. Kumar, et al., "Influence of degree of air oxidation and functionality on ensemble emission from nitrogen vacancy centers in nanodiamonds", Diamond and Related Materials **97**, 107431 (2019).

[66] B. Yu, B. Yang, H. Li, et al., "Effect of surface oxidation on photoluminescence of silicon vacancy color centers in the nanocrystalline diamond films", Applied Surface Science **552**, 149475 (2021).

[67] M. J. Degen, S. J. H. Loenen, H. P. Bartling, et al., "Entanglement of dark electron-nuclear spin defects in diamond", Nature Communications **12**, 3470 (2021).

[68] F. Jelezko, T. Gaebel, I. Popa, et al., "Observation of Coherent Oscillation of a Single Nuclear Spin and Realization of a Two-Qubit Conditional Quantum Gate", Physical Review Letters **93**, 130501 (2004).

[69] G. Waldherr, Y. Wang, S. Zaiser, et al., "Quantum error correction in a solid-state hybrid spin register", Nature **506**, 204–207 (2014).

[70] K. Nagata, K. Kuramitani, Y. Sekiguchi, and H. Kosaka, "Universal holonomic quantum gates over geometric spin qubits with polarised microwaves", Nature Communications **9**, 3227 (2018).

[71] D. M. Irber, F. Poggiali, F. Kong, et al., "Robust all-optical single-shot readout of nitrogen-vacancy centers in diamond", Nature Communications **12**, 532 (2021).

[72] J. L. Webb, L. Troise, N. W. Hansen, et al., "Detection of biological signals from a live mammalian muscle using an early stage diamond quantum sensor", Scientific Reports **11**, 1–11 (2021).

[73] K. Bian, W. Zheng, X. Zeng, et al., "Nanoscale electric-field imaging based on a quantum sensor and its charge-state control under ambient condition", Nature Communications **12**, 1–9 (2021).

[74] S. Sotoma, D. Terada, T. F. Segawa, et al., "Enrichment of ODMR-active nitrogen-vacancy centres in five-nanometre-sized detonation-synthesized nanodiamonds: Nanoprobes for temperature, angle and position", Scientific Reports **8**, 5463 (2018).

[75] D. Cohen, R. Nigmatullin, O. Kenneth, et al., "Utilising NV based quantum sensing for velocimetry at the nanoscale", Scientific Reports **10**, 1–13 (2020).

[76] R. Brouri, A. Beveratos, J.-P. Poizat, and P. Grangier, "Photon antibunching in the fluorescence of individual color centers in diamond", Optics Letters **25**, 1294 (2000).

[77] J. Tisler, G. Balasubramanian, B. Naydenov, et al., "Fluorescence and Spin Properties of Defects in Single Digit Nanodiamonds", ACS Nano **3**, 1959–1965 (2009).

[78] S. Gundacker and A. Heering, "The silicon photomultiplier: fundamentals and applications of a modern solid-state photon detector", Physics in Medicine and Biology **65**, 17TR01 (2020).

[79] A. Lacaita, F. Zappa, S. Bigliardi, and M. Manfredi, "On the bremsstrahlung origin of hot-carrier-induced photons in silicon devices", IEEE Transactions on Electron Devices **40**, 577–582 (1993).

[80] A. Ingargiola, M. Assanelli, I. Rech, et al., "Avalanche Current Measurements in SPADs by Means of Hot-Carrier Luminescence", IEEE Photonics Technology Letters **23**, 1319–1321 (2011).

[81] G. Orio, "Effetti della propagazione assistita da fotoni sulla risoluzione temporale di dispositivi SPAD in silicio: caratterizzazione sperimentale e simulazioni", PhD thesis (Politecnico di Milano, 2012).

[82] F. A. Inam, T. Gaebel, C. Bradac, et al., "Modification of spontaneous emission from nanodiamond colour centres on a structured surface", New Journal of Physics **13**, 073012 (2011).

[83] E. B. Flagg, A. Muller, J. W. Robertson, et al., "Resonantly driven coherent oscillations in a solid-state quantum emitter", Nature Physics **5**, 203–207 (2009).